2004-05-21

Modeling and Control of Surface Micromachined Thermal Actuators

Robert K. Messenger
Brigham Young University - Provo

MODELING AND CONTROL OF SURFACE MICROMACHINED THERMAL ACTUATORS

by

Robert K. Messenger

A thesis submitted to the faculty of

Brigham Young University

in partial fulfillment of the requirements for the degree of

Master of Science

Department of Mechanical Engineering

Brigham Young University

August 2004

BRIGHAM YOUNG UNIVERSITY

GRADUATE COMMITTEE APPROVAL

of a thesis submitted by

Robert K. Messenger

This thesis has been read by each member of the following graduate committee, and by majority vote has been found to be satisfactory

Date	Timothy W. McLain, Chair
Date	Larry L. Howell
Date.	John N. Harb

BRIGHAM YOUNG UNIVERSITY

As chair of the candidates's graduate committee, I have read the thesis of Robert K. Messenger in its final form and have found that (1) its format, citation, and bibliographic style are consistent and acceptable and fulfill university and department style requirements; (2) its illustrative materials including figures, tables, and charts are in place; and (3) the final manuscript is satisfactory to the graduate committee and is ready for submission to the university library.

Date

Timothy W. McLain
Chair, Graduate Committee

Accepted for the Department

Brent L. Adams
Graduate Coordinator

Accepted for the College

Douglas M. Chabries
Dean, College of Engineering and Technology

ABSTRACT

MODELING AND CONTROL OF SURFACE MICROMACHINED THERMAL

Robert K. Messenger
Department of Mechanical Engineering
Master of Science

A model that accurately describes the transient and steady-state response of thermal microactuators is desirable to provide guidance for design and operation. However, modeling the full response of thermal actuators is challenging due to the temperature-dependent material properties and nonlinear deformations that must be included to obtain accurate results. To meet these challenges a three-dimensional multi-physics nonlinear finite-element model was developed using commercial code. The Thermomechanical Inplane Microactuator (TIM) was chosen as a candidate application to validate the model. TIMs were fabricated using the SUMMiT V™ process and their response was measured using a high-speed camera. The TIMs were modeled and the model output was compared to the experimental data. The finite-element model predicts the steady-state response to within 0.74 percent and the transient response, as described by the time constant, to within 42 percent. The usefulness of the model was further demonstrated by its predicting that response time and energy consumption can

be reduced by actuating thermal microactuators with short-duration high-voltage pulses. This behavior was verified through testing.

Feedback control has proven useful in improving reliability and performance for a variety of systems. However there has been limited success implementing feedback control on surface micromachined MEMS devices. The inherent difficulties in sensing microscale phenomena complicate the development of an economical transducer that can accurately monitor the states of a surface micromachined system. We have demonstrated a simple and effective sensing strategy that uses the piezoresistive property of the polysilicon thin film of which surface micromachined MEMS devices are fabricated. The states of the device are monitored by measuring the change in resistance of flexible members which deflect as the device moves. Measurement of the output displacement of an in-plane thermal actuator is presented as a candidate application. The thermal actuator is constructed of angled pairs of expansion legs that are connected to a center shuttle. As current flows through the legs they heat up and expand. The expansion causes the center shuttle to displace in the direction the legs are angled. The center shuttle is also connected to a pair of sensing legs. Theses legs are identical to the expansion legs except that they are angled in the opposite direction. Three other leg pairs are electrically connected to the sensing legs in a Wheatstone bridge configuration. An excitation voltage is applied to the bridge, and as the sensing legs deflect with the center shuttle displacement, the resistance change across the legs can be determined by measuring the voltage across the bridge. While there still is a noise issue to be dealt with, this setup provides adequate signal strength to implement feedback control using off-chip analog circuitry. Implementation of proportional/integral control on the system is successfully demonstrated.

ACKNOWLEDGEMENTS

I would like to thank and acknowledge my graduate committee Dr. McLain, Dr. Howell, and Dr. Harb for providing guidance, funding, and encouragement. Fellow graduate students Scott Lyon, Jon Witwer, Craig Lusk and John Kennedy have also provided help in many different ways. Scott Lyon's insight were particularly necessary to the success of the piezoresisitive sensor.

Thanks needs to be given to my very patient wife, Amy and my two understanding sons, Andrew and Bennion.

Thanks also to the Ira and Mary Lou Fulton Supercomputing Center at Brigham Young University for providing the computing resources used in preparing this paper, and to Mike Baker at Sandia National Laboratories for providing me excellent experimental results.

TABLE OF CONTENTS

LIST OF FIGURES

CHAPTER 1 INTRODUCTION

1.1 Background

Microelectromechanical systems (MEMS) are a promising and active area of research, both in academia and industry. They consist of miniature embedded systems involving micromachined components or structures [1].

One of the most flexible methods for manufacturing MEMS is polysilicon surface micromachining. It consists of multiple, alternating layers of polysilicon thin films and sacrificial silicon oxide that are deposited on a silicon substrate. The number of layers depends on the process being used. For instance the Multi-User MEMS Process (MUMPs) uses up to two releasable layers while the Sandia Ultra-planar, Multi-level MEMS Technology (SUMMiT V) manufacturing process uses up to four. The layers are usually deposited using chemical vapor deposition (CVD). Each of the layers is lithographically patterned and etched before the next layer is deposited in order to create the desired geometry, and to anchor the layers to each other and to the substrate where desired. The final step is to release the polysilicon layers by etching away the sacrificial silicon oxide layers, which frees the remaining polysilicon structures allowing them to move [1]. Many useful and novel mechanisms have been manufactured using this method.

For most devices to be of use it is necessary to provide some actuating force. Thermal microactuators are a class of surface micromachined mechanisms that amplify the motion produced by the ohmic heating and consequent thermal expansion that is induced when a voltage is applied to the mechanism [2,3]. Thermal microactuators have many advantages over other microactuators used to motivate surface micromachined devices. Compared with electrostatic comb drives they are made of very simple, and consequently reliable geometries [4]. They also tend to use lower voltages, provide higher forces, and have smaller footprints than comb drives [5]. Unlike piezoelectric actuators, another microactuator technology [1], thermal microactuators can be constructed by the same surface micromachining process used to make the devices they actuate.

1.2 Motivation

Designing mechanical systems at the micro level poses some unique challenges with regard to reliability and robustness. For example, most surface micromachining processes typically maintain sub-micron tolerances, which if achieved with macro scale machining would be extraordinary. However, when critical feature sizes are designed to be 3 μm or less, tolerances in the range of tenths of a micrometer become significant. This is of particular importance when working with compliant mechanisms such as a TIM or a compliant bistable mechanism that the TIM is meant to actuate. The behavior of compliant mechanisms depend on how their various components deflect or deform, and are very sensitive to geometries such as lengths and cross sections [6].

Another example of reliability challenges in the micro environment is a problem known as stiction. Stiction is a combination of many surface forces that hamper the ability of a micro mechanism to move. Adhesion caused by capillary action left over from the release process, electrostatic attraction, van der Waals forces, and chemical forces have been identified as contributing to stiction [7]. These surface forces are much more dominant in micro environments than they are in macro environments.

Given these challenges it is difficult to reliably operate microdevices to get the desired behavior with much certainty. Due to the desirable characteristics of thermal microactuators, in this thesis we will develop modeling techniques that can accurately predict the behavior of thermal microactuators. However, because models are only as good as the parameters they are given, we will also develop a method to use the piezoresistive properties of polysilicon to monitor system parameters and implement feedback control of microdevices. This will allow us to compensate for variations in system parameters as well as improve performance.

1.3 Contributions

The research described in this thesis advances techniques for modeling thermal actuators and opens a new area of research in integrated piezoresistive sensing for MEMS. The significant physical phenomena that affect thermal actuator behavior have previously been identified and incorporated in models. I have incorporated those affects using sophisticated modeling techniques and validated the model with high-temporal-resolution data. The success of piezoresistive sensing to detect the displacement of a thermal actuator demonstrates the feasibility of using piezoresistive feedback sensors with MEMS. With its simple implementation, piezoresistive feedback of MEMS opens the potential for improved reliability, performance, and functionality for MEMS devices.

1.4 Document Organization

The body of this thesis is composed of two main parts which are found in Chapters 2 and 3. Chapter 2 describes the development of a nonlinear three-dimensional finite-element model of surface micromachined thermal actuators. Chapter 3 describes the implementation of feedback control on the output displacement of a thermal microactuator using piezoresistive sensing. Both Chap-

ters 2 and 3 are drawn from papers that, at the time this thesis was written, were being prepared for publication. As such they are both in a format that can stand alone and independent of the rest of the thesis. Only their abstracts, references, and appendices have been moved to be included with those of this thesis.

CHAPTER 2 MODELING THE RESPONSE OF THERMAL MICROACTUATORS

2.1 Introduction

Thermal microactuators, micro-scale mechanisms that amplify the motion produced by thermal expansion [2,3], have many advantages over other microactuators used to motivate surface micromachined devices. Compared with electrostatic comb drives they are made of very simple, and consequently reliable geometries [4]. They also tend to use lower voltages, provide higher forces, and have smaller footprints than comb drives [5]. Unlike piezoelectric actuators [1], thermal microactuators can be constructed by the same surface micromachining process used to make the devices they actuate.

The high output force and displacement characteristics of thermal microactuators make them ideally suited to meeting the power requirements of compliant, bistable devices [3,8]. Bistable devices, which have the advantageous attribute of having two stable equilibrium positions, do not require a power input to maintain either of their stable states. They only require actuation during transition between these two states [9,10].

The Thermomechanical Inplane Microactuator (TIM) is a thermal microactuator that produces a linear output force in the plane of the substrate [3]. It is constructed by suspending a shuttle off of the substrate with two symmetric arrays of thin beams. These beams are inclined in the direction of desired dis-

placement in a bent-beam or chevron shape. The beams are attached to bond pads which are anchored to the substrate as shown in Figure 2.1.

A voltage is applied across the two bond pads, which induces a current through the thin beams. The current generates ohmic heating, and as the temperature of the beams rise they expand. The lengthening of the beams causes buckling due to their ends being fixed in both rotation and lateral displacement. This

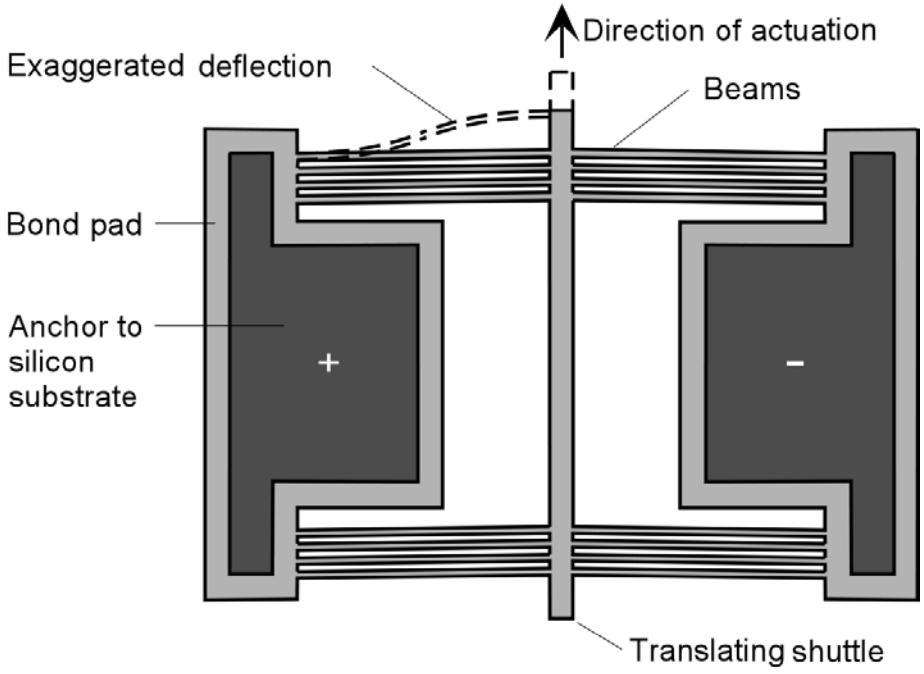

Figure 2.1: Diagram of the Thermomechanical Inplane Microactuator (TIM).

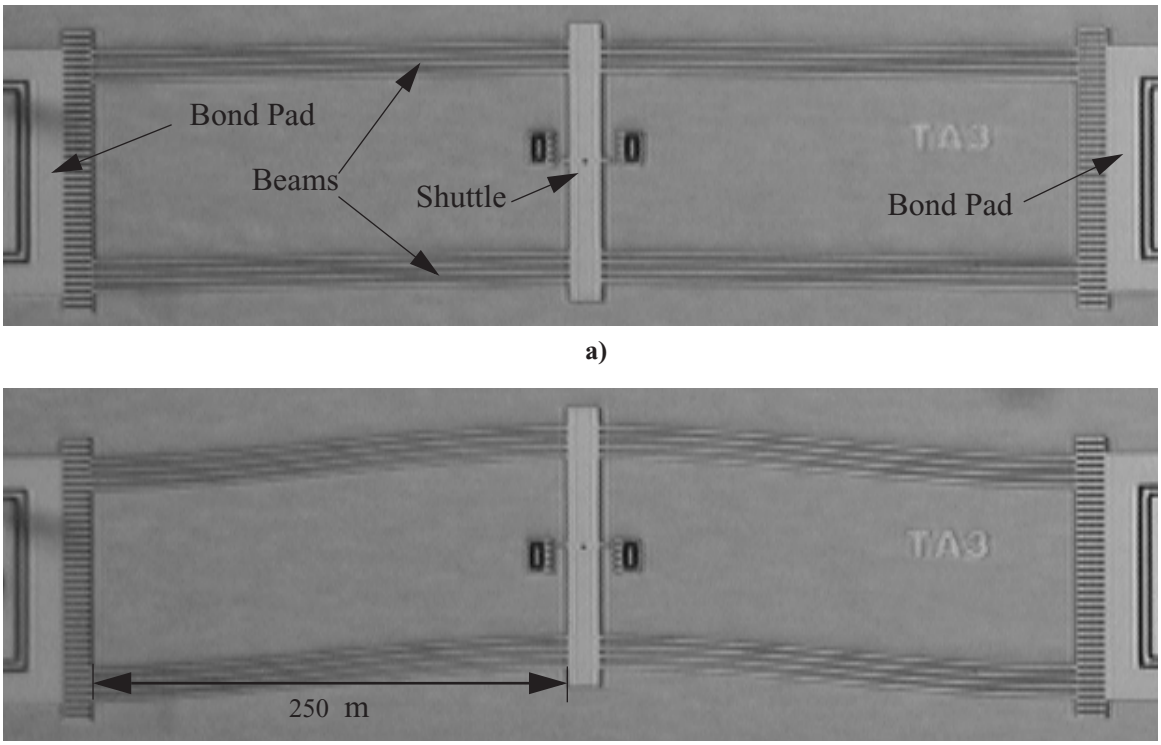

Figure 2.2: Optical micrograph of a Thermomechanical In-plane Microactuator (TIM) a) not actuated, and b) actuated.

buckling displaces the shuttle in the desired direction Figure 2.2. The geometry of the TIM is such that small increases in leg length due to thermal expansion are amplified into relatively large displacements of the center shuttle. For example, if the initial leg length is 250 μm and the increase in length due to thermal expansion is 0.5 μm, the resulting shuttle displacement is predicted to be 14.5 μm using finite-element-analysis. The output force is linearly scalable by the number of beam pairs [11].

Understanding the physics of TIMs provides for better designs, more efficient use, and consequentially better performance. Therefore it is desirable to have an accurate model describing the transient and steady-state behavior of TIMs. Some work has been done on modeling thermal microactuators, but while good results have been achieved modeling steady-state behavior [12,13,14], there has been limited success characterizing the dynamic or transient response [15,16].

This paper describes the development and results of an experimentally validated, three-dimensional, multi-physics, nonlinear, finite-element model that simulates the behavior of TIMs. Measurements of the transient response of TIMs were taken using a high-speed camera capturing 55,555 frames per second. Good correlation between the model simulation and the measured transient validates the model. The results of the simulation demonstrate the usefulness of a transient model by providing insights in how to operate TIMs with improved response time and energy efficiency.

2.2 Modeling the TIM

We have successfully used state-of-the-art finite-element code[1] to accurately model the significant physical processes that govern the transient response of TIMs. A sequentially coupled model was developed where the output of the electrothermal model is used as the input to the thermomechanical model. The electrothermal model calculates the temperature profile of the actuator by modeling the ohmic heating and heat conduction of the system. The thermomechanical model then uses the temperature profile to calculate the thermal expansion, and resulting deformation, of the actuator to obtain a prediction of the output displacement.

Electrothermal Model

To construct the model, the actuator geometry is modeled and meshed, along with the supporting substrate and surrounding air, in all three dimensions. The actuator is modeled with approximately 7,500 tetrahedral, coupled-field elements that can model both electrical and thermal physics.[2] The surrounding air and substrate are modeled with roughly 75,000 tetrahedral, thermal elements.[3] The electric current induced in the beams is calculated from the applied voltage and the actuator resistance. Voltage is applied using constant-voltage boundary

1. ANSYS 7.0, run on an SGI Origin 3800 Supercomputer.
2. ANSYS element SOLID98, keyopt 1.
3. ANSYS element SOLID87.

conditions on the top surfaces of both bond pads. The resistance is determined using the actuator geometry and the resistivity of the material. From the electric current, the ohmic heat generated in the beams is computed. The heat loss to the environment is calculated by modeling the heat conduction through the beams and bond pads to the substrate, and through the air to the substrate. A constant temperature boundary condition is applied to the bottom surface of the substrate. As demonstrated by others, the effects of free convection and radiation are not significant and are therefore not included in the model [12,16]. The heat conduction is a function of relative temperatures, the actuator geometry, and the material properties of the actuator and its surroundings. The material properties that affect the heat conduction are thermal conductivity, specific heat, and density.

Simplifying methods that are successfully used in steady-state modeling of the heat conduction through the air to the substrate cannot be used to model the transient response. Most others who have modeled thermal microactuators have used a micro-beam, thermal conduction shape factor [17]. The shape factor accounts for the heat transferred from the bottom and both vertical sides of the micro-beam to the effective projected area of the substrate that receives the heat. Unfortunately, these shape factors assume a fully developed temperature profile between the micro-beam and the substrate. They are suitable for steady-state simulations, but not for dynamic or transient studies. It is therefore necessary to do a full three-dimensional transient analysis to describe how the heat conduction through the air varies as a function of time. To state it another way, the shape factor has dynamics of its own as the system is moving toward steady state. A three-dimensional analysis is required to capture those dynamics.

To improve the efficiency of TIMs, the beams are often grouped together as closely as possible to decrease the heat loss to the environment. It is necessary to account for the heat conduction between the beams. A three-dimensional analysis allows us to incorporate this grouping effect in the model.

Temperature-Dependent Material Properties

During operation the temperature profile across the TIM varies greatly, from ambient temperature to about 1000 K. Therefore, an accurate model requires the inclusion of temperature dependency for all of the pertinent material properties that vary significantly over the temperature range. For example, not including the temperature dependency of the thermal conductivity for air inflates the peak temperatures in the profile along the beams by as much as 46 percent [11]. For the electro-thermal portion of the simulation we included the temperature dependency of resistivity, thermal conductivity, and specific heat of the polysilicon from which the actuator is made. We also included the temperature dependency for the thermal conductivity, specific heat, and density of the air surrounding the actuator. Due to the relatively high mass and thermal conductivity of the mono-crystalline silicon substrate, its temperature does not vary greatly and can therefore be accurately modeled with constant thermal properties. In the thermomechanical portion of the model, the temperature dependence of the coefficient of thermal expansion of polysilicon is included.

All temperature dependent relationships are taken from published data. In the cases where the relationships are listed as functions, a fourth-order polynomial is fit to the function and entered into the finite-element program. The finite-element program calculates the material properties at various temperatures to create a lookup table. The resistivity of polysilicon is modeled to increase linearly from its room temperature value as the temperature increases. For the material properties that are published as tables, the table values are entered manually. A comprehensive list of the material property values used, along with the references from which they are taken, are found in Tables A.1 through A.3 in Appendix A.

Due to the temperature dependence of the material properties, the electro-thermal simulation requires a nonlinear solution using a Newton-Raphson algorithm. To maintain accuracy and temporal resolution, the model converges to a solution about every 1 μs. The time integration is accomplished using a New-

mark method. The temperature profile across the actuator beams through time can be extracted from the solution to the electrothermal simulation.

Results of the Electrothermal Model

We have simulated a TIM with geometry and dimensions as shown in Figure 2.3 and Table 2.1. This TIM was also fabricated using the SUMMiT V™ process for experimental validation of the model.

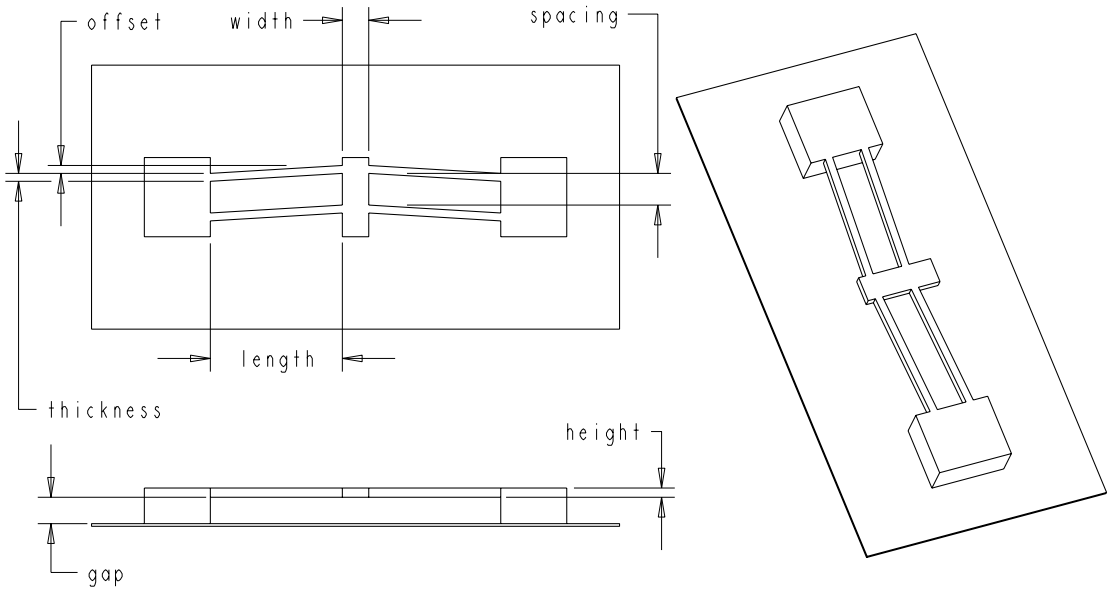

Figure 2.3: Geometry of the SUMMiT V™ TIM.

Table 2.1: Dimensions used in the simulation of the TIM described in Figure 2.3.

length	height	gap	thickness	spacing	offset	width
248 μm	2.52 μm	2.04 μm	2.04 μm	2.8 μm	4.8 μm [a]	17 μm

a. Including a designed 3.0 μm offset and an additional measured 1.8 μm offset resulting from residual stress remaining from fabrication.

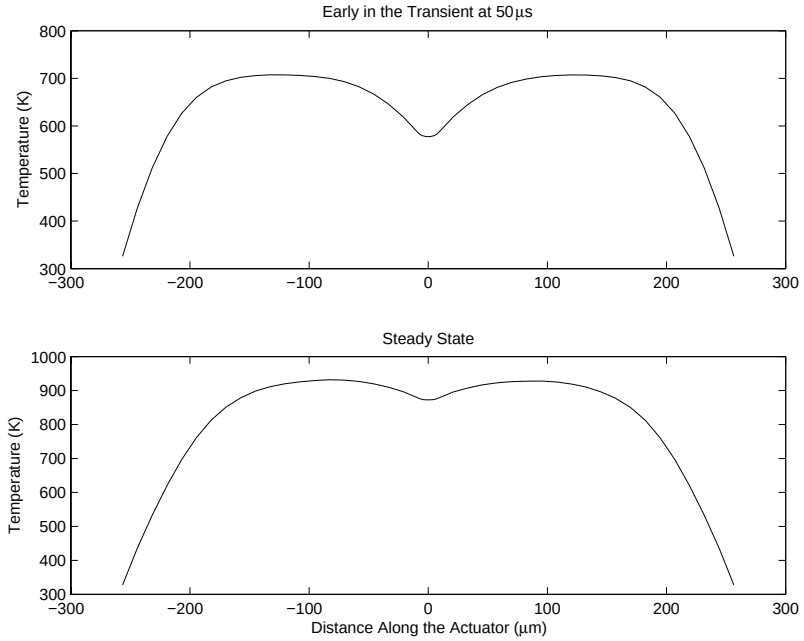

Figure 2.4: Temperature profiles across the beams and shuttle of the actuator.

Two temperature profiles, extracted from the electrothermal simulation, are shown in Figure 2.4. One profile is taken early in the transient and the other is taken at steady state. As expected, the temperatures are depressed near where the beams connect to the bond pads. This is due to the bond pads being held near ambient temperature by the large substrate they are in contact with. The temperatures are also lower across the shuttle, in part due to the larger area the shuttle has facing the substrate facilitating greater conduction, and the much lower ohmic heating taking place. However, it can be noted that the shuttle temperatures are lower early in the transient than they are at steady state. This is due to the shuttle having mass and specific heat which cause the shuttle to heat up more slowly than the beams. The temperature profile along the beams is also more rounded at steady state than it is early in the transient when the heat generated in the beams has not had time to conduct to the shuttle and bond pads.

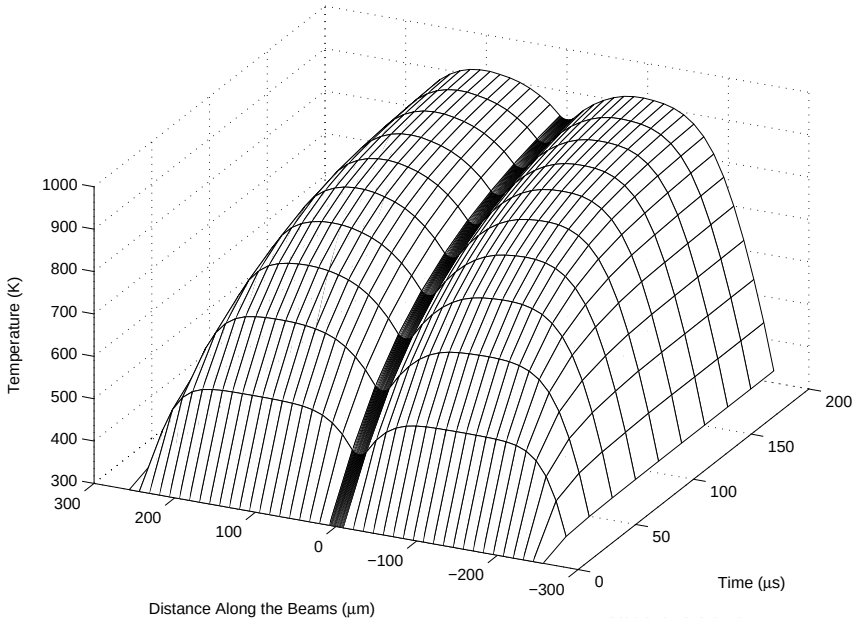

Figure 2.5: Temperature profile of a beam pair and connecting shuttle through time.

Figure 2.5 shows a plot of the temperature profile as it changes through time. Just as in Figure 2.4 the temperature profile is lower in the middle of the actuator where the shuttle is and at the ends near the bond pads. The profile also becomes more rounded as time increases and the actuator approaches steady state. The rise in temperature versus time is suggestive of a first-order response that is typical of thermal systems described by the heat equation:

$$\frac{\partial^2 T}{\partial x^2} + \frac{\partial^2 T}{\partial y^2} + \frac{\partial^2 T}{\partial z^2} + \frac{q^{gen}}{k} = \frac{1}{\alpha}\frac{\partial T}{\partial t}.$$

In the heat equation, the rate of change of temperature, $\frac{\partial T}{\partial t}$, is proportional to the sum of the net heat conduction, $\frac{\partial^2 T}{\partial x^2} + \frac{\partial^2 T}{\partial y^2} + \frac{\partial^2 T}{\partial z^2}$, and the internal heat generation, q^{gen}, where k and α are the thermal conductivity and thermal diffusivity. As the temperature rises, the heat conduction transfers more heat to the surroundings until it is equal to the internal heat generation. The change in temperature slows until it converges at steady state. Thus the earlier the system is in its transient response, the faster the temperature will change.

In the case of thermal actuators, a desired output displacement corresponds to a desired average temperature of the temperature profile along the beams. Exploiting our knowledge of the electrothermal transient of TIMs enables us to reach that desired temperature, and therefore deflection, faster by operating the actuator in the early part of the transient response. Operating in the early part of the transient also results in less energy loss from the beams to the center shuttle or to the surroundings. As will be shown later, this leads to more efficient energy usage as heating of the center shuttle and the surroundings does not contribute to displacing the shuttle.

Thermomechanical Model

The temperatures obtained in the electrothermal simulation, at various times throughout the transient, are used as inputs to the thermomechanical model. The deformation of the actuator is only affected by its surroundings in that they hold the bond pads fixed. Rather than modeling the surrounding air and substrate, it is only necessary to apply a zero displacement boundary condition on the bottom of the bond pads. The TIM is modeled with tetrahedral structural elements[1] using the same mesh used in the electrothermal simulation. The thermomechanical simulation also requires a nonlinear solution due both to the large deformations imposed upon the actuator by the thermal expansion of the beams and to the temperature dependency of the thermal expansion coefficient. The temperatures from the electrothermal simulation are input into their corresponding geometries as body loads of the elements modeling the actuator. Using the temperature-dependent thermal expansion coefficient (see Table A.1), the lengthening of the beams can be calculated by the finite-element program. The buckling of the beams is calculated from their lengthening and their fixed-end

1. ANSYS element SOLID92.

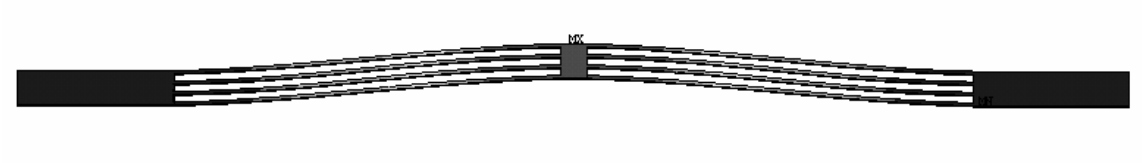

Figure 2.6: Finite element analysis output of the actuated TIM.

conditions. An image of the deformed TIM produced by the finite-element software is shown in Figure 2.6.

A point on the shuttle is tracked through time to represent the TIM's output displacement. The displacement step response of the TIM shuttle is plotted in Figure 2.7. The typical first-order response described above is also evident in the thermomechanical transient. However, it is distorted by the nonlinear, large-angle deflections of the TIM. A resonance at about 250 kHz can also be noted in the simulated response. However this resonance is much faster than the dominating, first-order response, and is low enough in amplitude to be of secondary significance. Also, as there is no damping in the model this resonance is likely to be amplified compared to the real system. The finite-element software changes the integration time step depending on how fast the solution is converging. Because the vibration does not change in frequency as the time step changes, the oscillation is unlikely to be a numerical artifact related to the time step. We also simulated a TIM with a shuttle that is ten times as massive by making it ten times wider. This simulation had a similar resonance in the results except that it vibrated at about 170 kHz. Considering the change in mass and stiffness of the system by making the shuttle ten times wider, this change in frequency is consistent with the expected change in mechanical resonance.

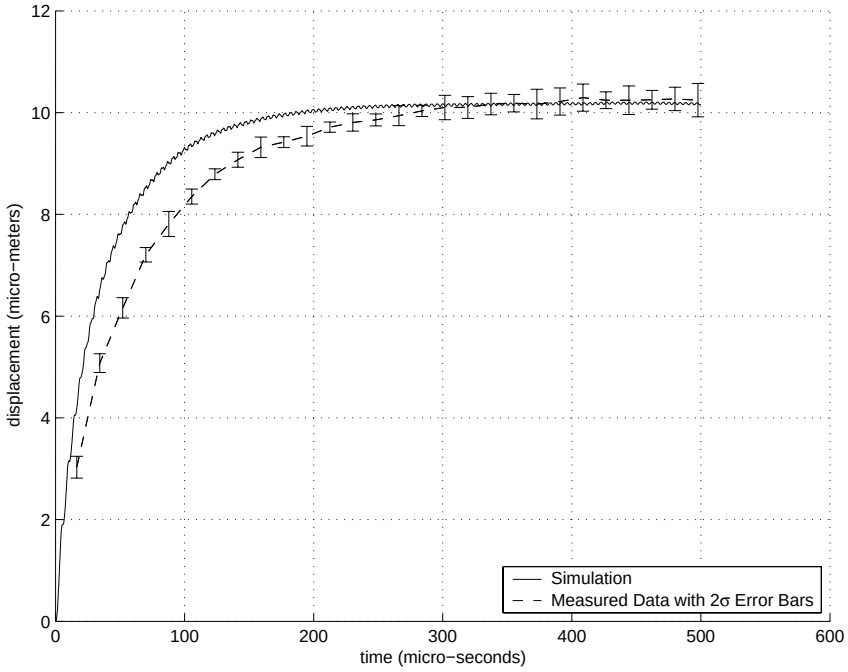

Figure 2.7: Displacement versus time plot, for a step response, of both simulation and experimental results.

2.3 Experimental Results

To validate the transient numeric model, a TIM was manufactured using the SUMMiT V™ surface micromachining process at Sandia National Laboratories. The actuator that was fabricated and tested is described in Figure 2.3 and Table 2.1. The part was released in hydrofluoric acid and dried using a supercritical carbon dioxide drying process. To measure the actuator displacement versus time, a Phantom V5 high-speed digital camera was configured to capture images of the actuation cycle at a speed of 55,555 frames per second, or one image every 18 μs. The actuator was driven with square waves of varying pulse widths, from 600 to 50 μs. To ensure timing accuracy, the high-speed camera was synchronized to the output of the pulse generator that provided the actuation drive signal. The actuator operating voltage and current were measured using an Agilent 100 MHz digital oscilloscope, with the current being determined by measuring the voltage

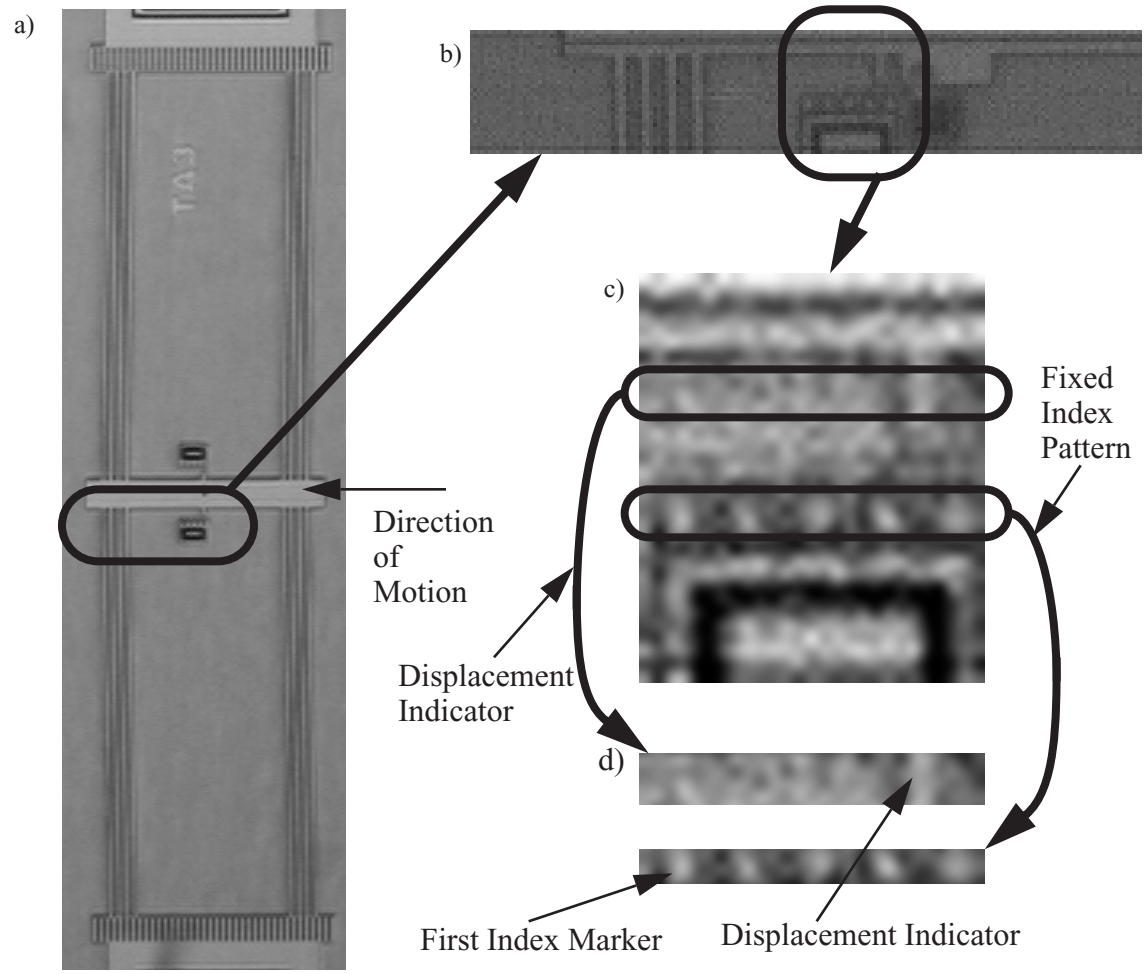

Figure 2.8: Steps used to process video frames: a) actuator layout for reader orientation; b) unmodified frame from-high speed camera; c) crop, resize, and blur; d) crop displacement indicator and fixed index pattern.

drop across a 100 ohm resistor in series with the actuator. The recorded voltage drop across the actuator versus time was used as the input voltage for the simulations.

The frames taken during the actuation cycles were processed to measure the displacement of the TIM shuttle through time. The frames were enhanced to provide more accurate measurements by increasing the contrast, resizing by 10 times, and applying a gaussian blur with a radius of 3 pixels. The fixed index pattern and the moveable displacement indicator were isolated by cropping those two features (see Figure 2.8). The resulting images were converted to numeric arrays corresponding to the gray-scale value of each pixel. The mean of each col-

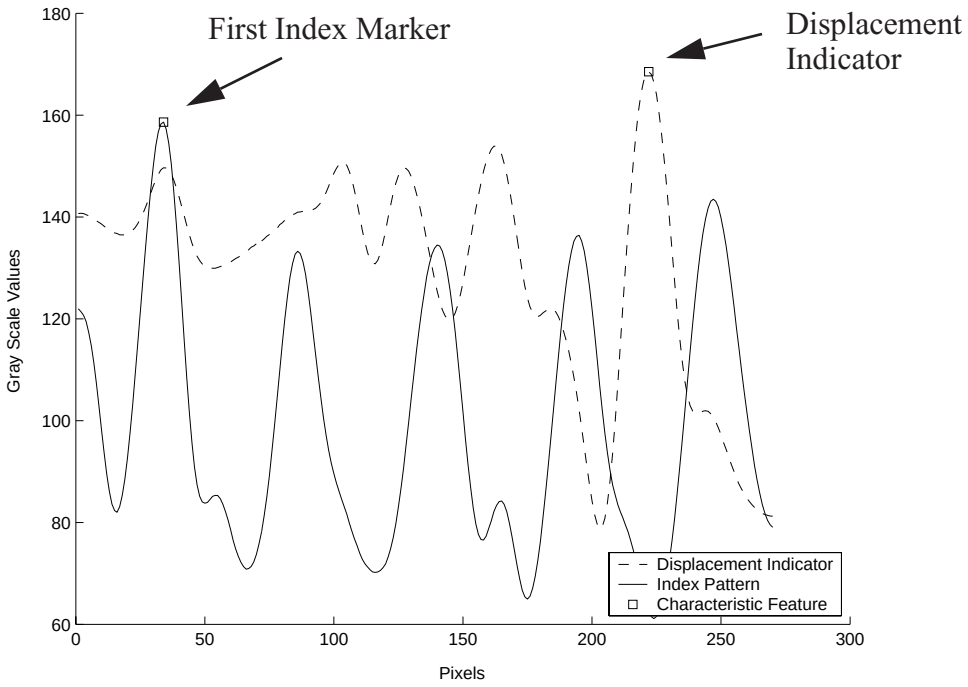

Figure 2.9: Gray-scale profile of a processed video frame.

umn, in the arrays, is calculated to create a gray-scale profile for each frame. An example gray-scale profile corresponding to the images in Figure 2.8 is shown in Figure 2.9. Minimums and maximums in the profile correspond to shadows and bright spots in the images. Enlarging the image and applying a gaussian blur provides a much smoother profile, which facilitates accurate measurements of the locations of the minimums and maximums. By choosing characteristic shadows or bright spots in both images, the movement of the displacement indicator can be determined relative to the index pattern with sub-pixel accuracy. The image is spatially calibrated by superimposing the design geometry on top of the image and iteratively resizing the design geometry until it matches the frame geometry. In this way a calibration factor in μm per pixel can be obtained, and the displacement measurements can be converted from pixels to μm.

The TIM was given 12.5 V square pulses for 600 μs every 1.3 ms. Ten of these cycles were measured using the above technique, and the mean and standard deviation of the cycles were calculated for comparison with the simulation results. The resulting data are plotted in Figure 2.7 with two standard deviation,

or approximately 95 percent confidence, error bars for each of the time steps measured.

2.4 Model Validation

The simulated TIM was given the same 12.5 V square pulse that the physical TIM was given. Good correlation was found between the simulation and the measured data as can be seen in Figure 2.7. The time constant for the simulation was off from the measured data by about 42 percent at 33.1 μs compared to 57.6 μs. The steady-state value was off by less than 1 percent at 10.18 μm versus 10.26 μm for the modeled and measured data, respectively.

From comparing the simulation results with experimental results, it is evident, as others have also shown [15,16], that it is difficult to accurately predict the transient behavior of thermal microactuators. The relatively small disparities between the model prediction and experimental results for steady-state response could easily be caused by uncertainties in the input parameters to the model. Parameters that affect the steady-state simulation include the material properties of resistivity and thermal expansion of polysilicon, and thermal conductivity of mono and polysilicon and air. Also affecting the predicted steady-state output are the dimensions of the actuator, particularly the cross sectional dimensions of the beams. All of these parameters have some uncertainty which may effect the accuracy of the prediction. For instance the width of the beams was determined by taking the designed thickness of 2.2 μm and subtracting the mean overetch. For the lot this actuator was fabricated with, the mean overetch was 0.16 μm. However, the maximum overetch measured with the lot was 0.23 μm. That provides a possible variation, from the mean width of the beam, of over 3 percent. This variation, in turn, affects the predicted steady-state output of the TIM by 1.5 percent. This demonstrates, as is always the case, that accurate input parameters are necessary for an accurate model. Unfortunately, it becomes increasingly difficult to determine the input parameters accurately as the spatial scales become smaller. The small spatial scales and fast time scales also make measuring the experimental data for model validation difficult, as demonstrated by the error bars in

Figure 2.7. This model shows good correlation for steady-state predictions because the model predicts accurately to within the uncertainty from the model inputs parameters and the measurements.

The disparity in the transient response cannot be entirely accounted for by the uncertainty of the input parameters and measurements. The only parameters that would affect the transient without also significantly affecting the steady-state response are the density and specific heat of both air and polysilicon. Even with micro scale devices, it seems dubious that there is enough uncertainty in those four parameters to account for the 42 percent disparity between the predicted and measured time constants. However, the friction and dissipative forces that are definitely present, but not included in the model, may be able to account for the dissimilarity between prediction and measurement. It would be unreasonable to assume there is no internal damping in the actuator itself, or the possibility of coulomb friction from the actuator rubbing on the substrate. Unfortunately, friction is very difficult to characterize in the general sense as it tends to be dependent on particular influences, such as release method, fabrication variables, grain orientation, and even environmental variables such as relative humidity. Without modifying the model for each particular case to match the experimental results, the results produced when the model neglects friction are still useful. They provide lower bounds on response time, and can be used for feedback control design where underestimating the damping is typically done to ensure stability.

2.5 Pulsed Input

As suggested above, large performance gains can be attained by operating TIMs in the early part of their transient response. To further validate that the finite-element model adequately predicts TIM performance during the transient and to quantify the improvements that can be gained, additional simulations and experiments were performed. These investigated the effect of short-duration, high-voltage pulses as inputs to the TIM.

It is possible to safely operate TIMs in the early part of the transient response by driving them with short-duration high-voltage pulses. If a constant

over voltage is applied to the TIM, it will burn out as the polysilicon is heated beyond its melting point. However, if the voltage is removed when the TIM reaches the desired displacement, then the TIM will cool off and relax to its initial state. This is an ideal way to drive bistable or latching mechanisms, which do not require any holding force once they are actuated into their equilibrium position.

Once again, not only does operating TIMs with short-duration high-voltage pulses decrease response time, it also increases energy efficiency. Operated this way, the TIM will spend less time at elevated temperatures, when conduction to the surroundings is greatest. A TIM actuated to steady state by a constant input spends the majority of its cycle time at those elevated temperatures when the maximum amount of energy is lost to the surroundings. Also, less energy is lost heating up the shuttle, which does not contribute to the thermal expansion of the beams and therefore does not contribute to the output displacement of the actuator.

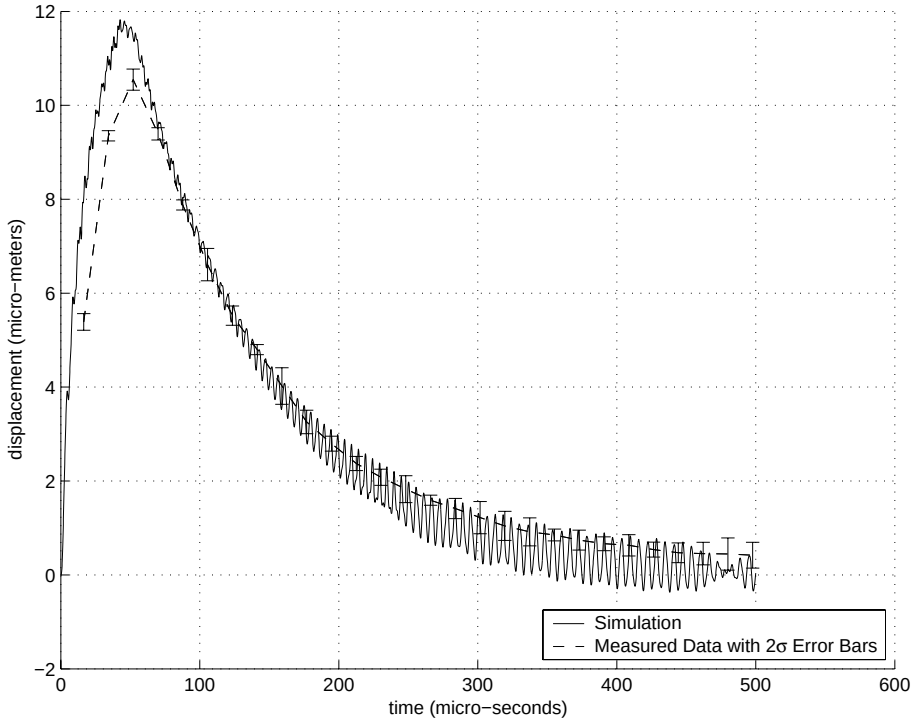

Figure 2.10: Displacement versus time plot of both simulation and experimental data for a TIM actuated with a short-duration, high-voltage pulse.

Figure 2.10 shows the measured and simulated results for the TIM, described in Figure 2.3 and Table 2.1, actuated with a 19.5 V pulse applied for 50 μs. It took approximately 50 μs to reach the same deflection as a steady-state application of 12.5 V (see Figure 2.7).

The accuracy with which the model predicts the TIM's response to the pulse is similar to that of the step response. It does a good job of predicting the response close to steady state, but only does an adequate job of predicting behavior early in the transient. As can be seen in Figure 2.10 the predicted maximum displacement of 12.1 μm overestimates the measured displacement of 10.5 μm by about 15 percent. Once again, the presence of friction is a possible cause of the discrepancy.

Additionally, further experiments were run at various pulse magnitudes with the same desired maximum output displacement. The response time, power requirements, and energy consumption were measured and are listed in Table 2.2.

The numbers reflect the response for a maximum output displacement of 12 μm. These results demonstrate that response time and energy consumption are reduced as the actuation pulse increases in magnitude.

Table 2.2: Experimental results of a TIM driven with various pulses to the same maximum output displacement.

Input Voltage (V)	Response Time (μs)	Mean Power Required (mW)	Total Energy Required (mJ)
12.5 (Steady-State)	600	275	165
13.6	300	367	110
16.4	75	574	43
19.5	50	761	38

2.6 Conclusions

Thermomechanical Inplane Microactuators (TIMs) have successfully been used in applications that require high output force and displacement, small footprint, and low operating voltages. An experimentally validated three-dimensional multi-physics nonlinear finite-element model that accurately describes both the steady-state and transient response of TIMs has been developed. A three-dimensional model was used to capture the dynamics of the heat conduction through the air to the substrate, and to account for the heat conduction between adjacent beams. Also, temperature dependent material properties were used to accurately model the TIM.

A clear description of the TIM transient was made by taking measurements from high-speed video frames taken of a TIM during actuation. Simulation results from the finite-element model were compared with the experimental data. Good correlation between the numeric and experimental results validates the finite-element model.

Using the finite-element model the transient response of the TIM can be simulated to investigate the practicality of driving the TIMs with short-duration, high-voltage pulses.

CHAPTER 3 FEEDBACK CONTROL USING PIEZORESISTIVE SENSING

3.1 Introduction and Background

Microelectromechanical systems (MEMS) have the potential to make large advancements in a variety of important technology fields, and to open up fields that would not be possible without them [1]. Devices created at the micro scale have characteristics that give them significant advantages over the analogous macro devices they replace. Compared with macro devices they can have faster responses, smaller form factors, and lower power requirements. Additionally, fabricating MEMS by leveraging mature semiconductor manufacturing processes, including the inherent economies of scale, can greatly reduce costs.

Unfortunately micro scale devices also have some inherent issues that have limited the implementation of MEMS on a wider scale. One such issue is device variability. This variability can cause substantial differences in performance and reliability from one device to the next. Sources of variability include stiction, uncertainty in material properties, and fabrication tolerances.

One proposed solution to the problem of device variability is feedback control. Feedback control has proven very effective at the macro scale to provide robust and reliable operation for a variety of applications. It also has the potential to significantly improve system performance. For example, in actuating a bistable switch, feedback control of the position of the switch may help the reliability and

efficiency of the system by ensuring that switch is moved past its unstable equilibrium position.

However, at the micro level and particularly with surface micromachined devices, implementation of feedback control faces distinct challenges imposed by size and complexity constraints. For example, due to the small size of the devices, the signal-to-noise ratio produced by the feedback transducers is usually quite poor. The typical way to compensate for this is to fabricate the control circuitry on the same die as the MEMS. Unfortunately, this requires custom fabrication processes that can be very expensive to develop and run, usually requires compromises in both the MEMS and circuitry design, and may not be flexible enough to transfer to future products.

Another solution that has been used in laboratory setups is off-chip sensing. Devices such as Laser Doppler Vibrometers [18] and Laser Interferometers [19] have been used to provide accurate real-time measurements of microdevice operations. However, these are not desirable solutions for anything other than prototypes or very expensive, low-volume products.

Despite these difficulties, feedback control has been used successfully to overcome the large uncertainties inherent to MEMS devices. It has been used to compensate for the hysteresis of shape memory alloy (SMA) microactuators using the electrical resistance of the SMA, which reflects its state [20]. It has also been shown that feedback control can be used to control the nonlinear behavior of piezoelectric PZT microactuators [21].

One major application where the use of feedback control of MEMS devices is being investigated and where much work has been done is hard drive read/write head positioning. Typically a dual-stage actuation is used with the fine-control stage being accomplished with a MEMS device [22,23,24,25,26,27]. The cost reduction involved with the batch fabrication of MEMS devices compared to current solutions is particularly motivating.

Thermal Microactuators

The Thermomechanical Inplane Microactuator (TIM) is a thermal microactuator that produces a linear output force in the plane of the substrate [3]. It is constructed by suspending a shuttle off of the substrate with two symmetric arrays of thin beams. These beams are inclined in the direction of desired displacement in a bent-beam or chevron shape. The beams are attached to bond pads which are anchored to the substrate as shown in Figure 3.1.

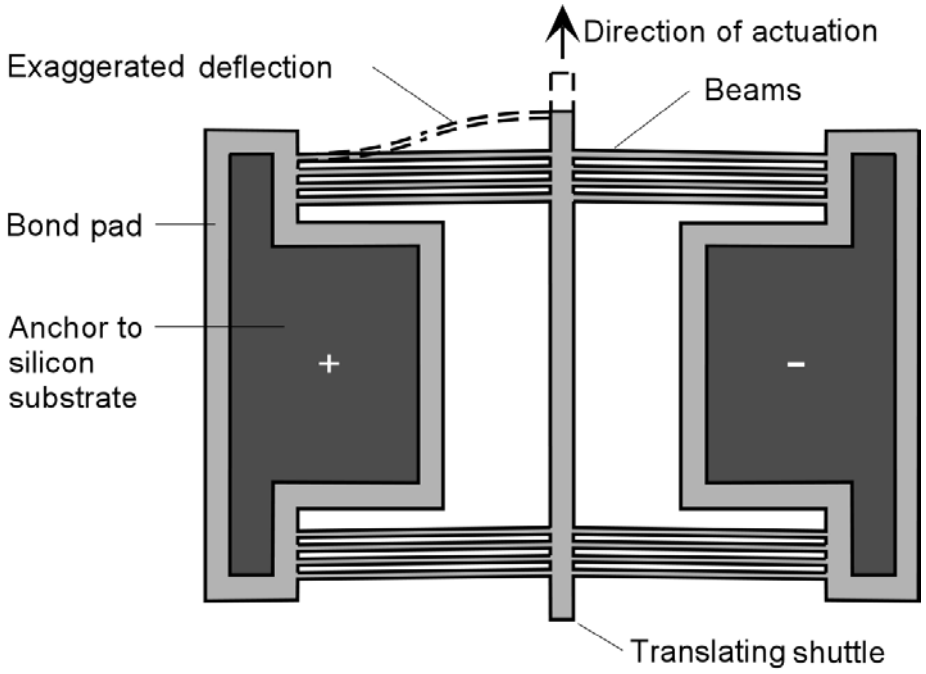

Figure 3.1: Diagram of the Thermomechanical In-plane Microactuator (TIM).

A voltage is applied across the two bond pads, which induces a current through the thin beams. The current generates ohmic heating, and as the temperature of the beams rise they expand. The lengthening of the beams causes buckling due to their ends being fixed in both rotation and lateral displacement. This buckling displaces the shuttle in the desired direction as shown in Figure 3.2. The geometry of the TIM is such that small increases in leg length due to thermal expansion are amplified into relatively large displacements of the center shuttle. For example, if the initial leg length is 250 μm and the increase in length due to

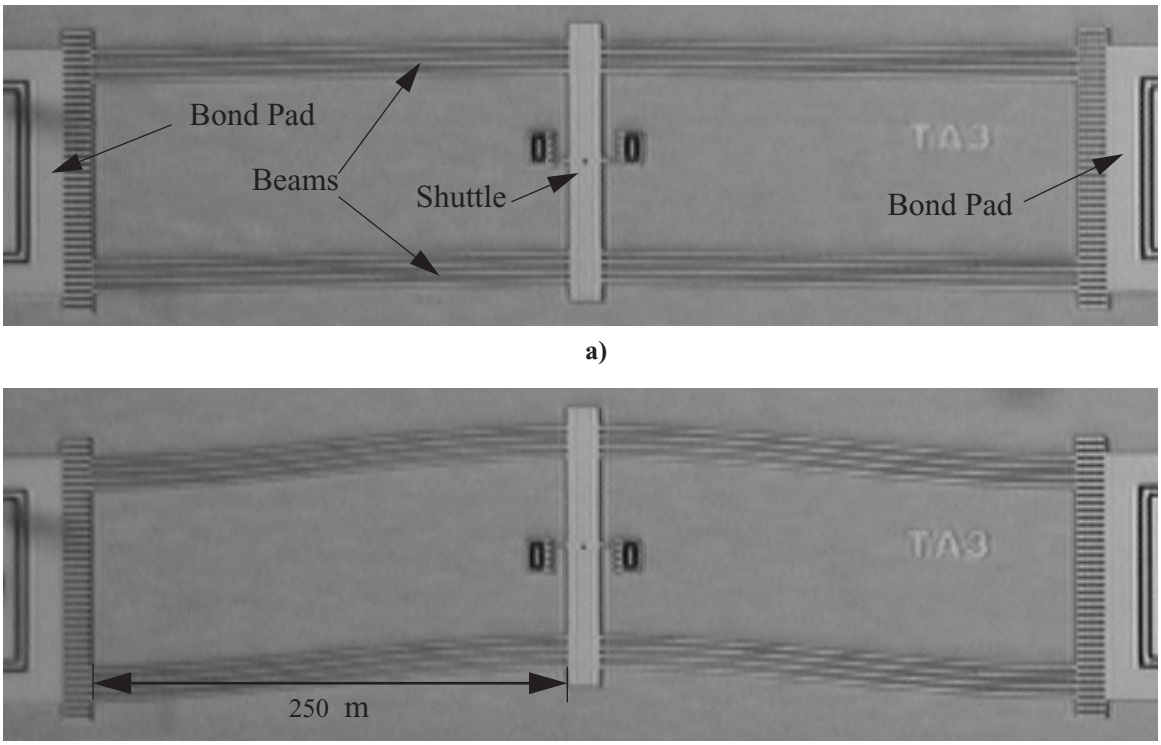

Figure 3.2: Optical micrograph of a Thermomechanical In-plane Microactuator (TIM) a) not actuated, and b) actuated.

thermal expansion is 0.5 μm, the resulting shuttle displacement is predicted to be 14.5 μm using finite-element-analysis. The output force is linearly scalable by the number of beam pairs [11].

The desirable attributes of thermal microactuators, specifically the TIM, have been demonstrated in the literature [8]. As such the TIM has been chosen as a candidate application for the development of a MEMS feedback control system. Research has been done on the control of many types of microactuators from electrostatic "comb" drives [22,23,24,28], to piezoelectric [21,22], to SMA [20], but little if any has been done on the control of microactuators that use thermal expansion as the driving force.

Piezoresistivity

To sense the output displacement of the TIM it is proposed to use the piezoresistive properties of polysilicon, of which the device is fabricated. Piezore-

sistive sensing may provide for significant advantages over other MEMS sensing technologies in both simplicity of design geometry and manufacture, and in output signal strength. Another advantage is that measuring resistance is an inherently DC setup while the dominant on-chip sensing technology, capacitive sensing, is inherently AC, making the supporting circuitry more complex.

While there is no published work on using the piezoresistive properties of polysilicon films to measure small displacements, there is significant work on using the phenomenon to measure other small effects. It has been used to detect acoustic waves in a microphone assembled on a single chip [29], to detect forces in the cantilevers of atomic force microscopes [30], and as a Wheatstone bridge pressure sensor for in vivo blood pressure sensing [31].

3.2 Piezoresistive Sensor

Piezoresistivity is an attribute of certain materials that change in electrical resistivity when a mechanical stress is applied. To design a piezoresistive sensor that measures in-plane displacement, a device must be designed that deforms as it is moved in-plane so that the stress increases in a consistent and repeatable way. As the stress changes the electrical resistance of the device changes due to the piezoresistive effect. Compliant mechanisms are well matched to piezoresistive sensing because compliant mechanisms gain all or part of their motion through the deflection of one or more of their members [6]. As such it may be possible to design a compliant mechanism with the sensor integrated into the mechanism so that it directly measures the stress of the flexible members of the device as the flexible members provide the functionality for the device. However, to simplify this study we will use a sensor that is not integral to the TIM we are trying to control. If the sensor were an integral part of the TIM we could not isolate the TIM actuation signal from the constant excitation voltage used to measure the resistance change across the sensor.

The Piezoresistive Micro-Displacement Transducer (PMT)

The Piezoresistive Micro-Displacement Transducer (PMT) is a set of four TIM beam pairs arranged in a Wheatstone bridge configuration. Three beam pairs are fixed so they cannot move while the fourth, or sensing beam pair is connected the moving object we are measuring. In this case the sensing beams are connected to the shuttle of a TIM as shown in Figure 3.3. An excitation voltage is applied across the bridge and the change in resistance of the sensing beams compared to the other beams can be measured as a voltage difference across the bridge (voltage between points *a* and *b* in Figure 3.3). It is necessary to have the reference legs of the bridge be constructed of "dummy" beams that are constructed identically to sensing beams. This ensures that all four beam pairs undergo the same increase in temperature due to the excitation voltage inducing a current through them, and therefore allowing all thermal effects on resistance to be cancelled out. If standard resistors are substituted for the reference legs of the bridge the sensor output will not reflect just the piezoresistive effect, but the thermal resistance change of the sensing beams as well.

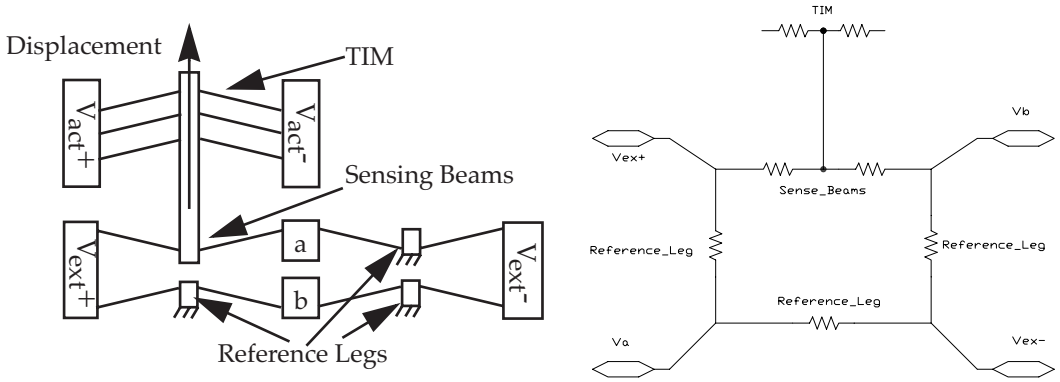

Figure 3.3: Layout and equivalent electrical schematic of the Piezoresistive Microdisplacement Transducer (PMT) connected to a TIM.

To provide a consistent increase in stress as the PMT is displaced, the sensing beams are inclined away from the direction of desired motion. The sensing beams apply a force on the object it is connected to because the excitation voltage

causes the beams to heat up and expand. As the object deflects the sensing beams opposite to the force they are applying the stresses inside the beams increase. A scanning electron micrograph of the PMT connected to a TIM is in Figure 3.4.

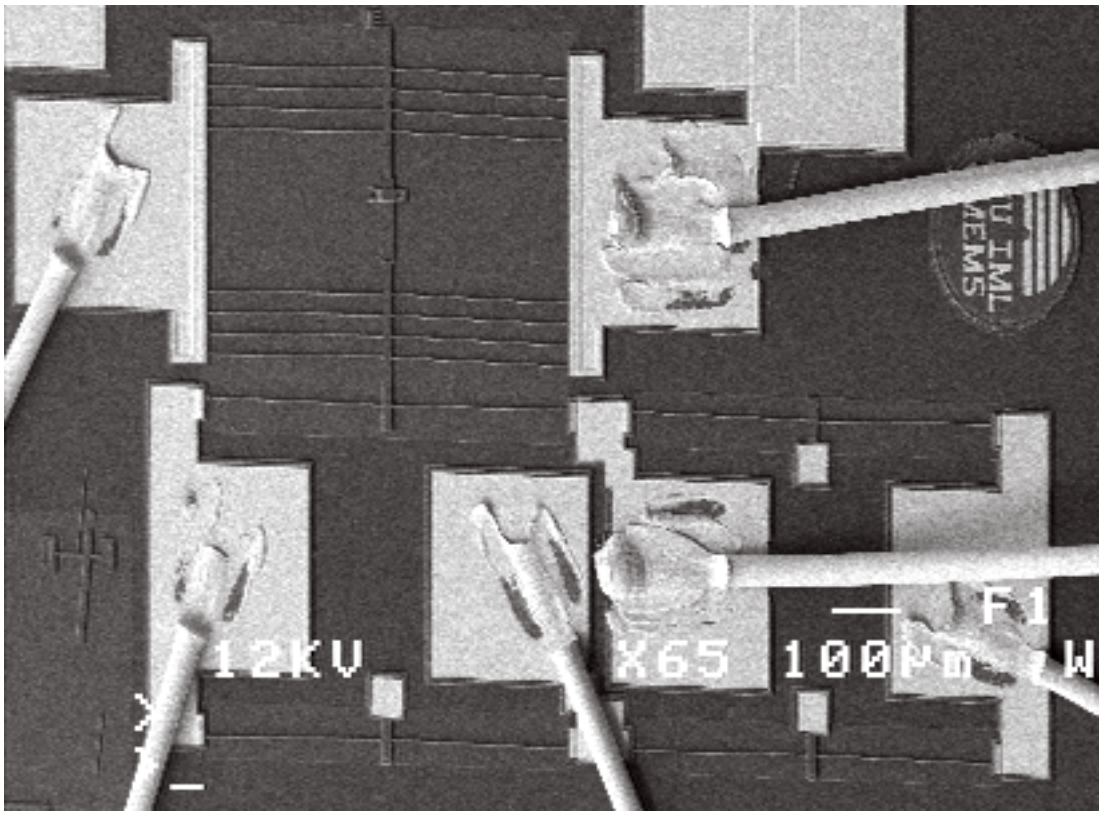

Figure 3.4: Scanning electron micrograph of a PMT connected to a TIM.

A calibration curve was obtained for the PMT by measuring the TIM displacement using a scanning electron microscope and measuring the output of the PMT. The sensor shows good linearity and little hysteresis. The sensor output versus displacement and a linear fit of the data are shown in Figure 3.5.

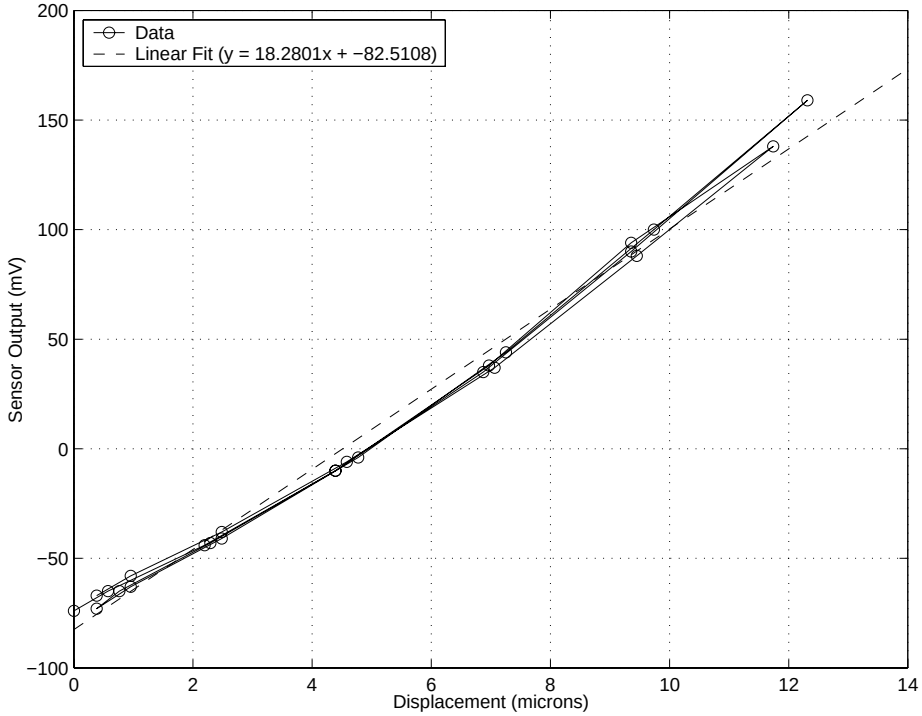

Figure 3.5: Calibration curve for the PMT

Measuring the Displacement of a TIM with a PMT

Because there are no electrically insulating structural layers in standard surface micromachining processes such as the MUMPs [32] process it is not possible to mechanically connect and electrically isolate the TIM and the PMT. It is therefore necessary to provide a way to power and monitor the system so that the sensor output is not affected by the electrical input to the TIM. One way to do this is to use a floating power supply, or one that is not connected to a ground, to supply the excitation voltage to the Wheatstone bridge. When excited this way a constant voltage potential across the bridge will be maintained, but the voltage of the bridge in reference to earth ground will move up and down with the electrical input driving the TIM. This is acceptable because we only need to measure the voltage potential across the bridge at points a and b (see Figure 3.3) to know the resistance change in the sensing beams.

A TIM connected to a PMT was driven with various dynamic inputs to validate the approach of using a floating power supply for an excitation voltage. The sensor output can be seen in Figure 3.6. The PMT is able to produce an output voltage proportional to the displacement of the TIM, however there is an issue with periodic interference spikes at about 70 to 100 Hz as can be seen in Figure 3.6. We are confident that the phenomenon is actually interference and not just a measurement of the TIM motion for two reasons. Examining the signal driving the TIM shows that it is well conditioned and therefore could not be inducing the motion indicated by the interference. Additionally, when driving the TIM with a signal of similar frequency to that of the spikes the TIM is visibly blurred when examined with an optical microscope. This blurring is not evident when the TIM is driven with a constant input.

The interference amplitude is significant compared to the sensor range and is therefore an issue that needs to be addressed. We have been unsuccessful so far

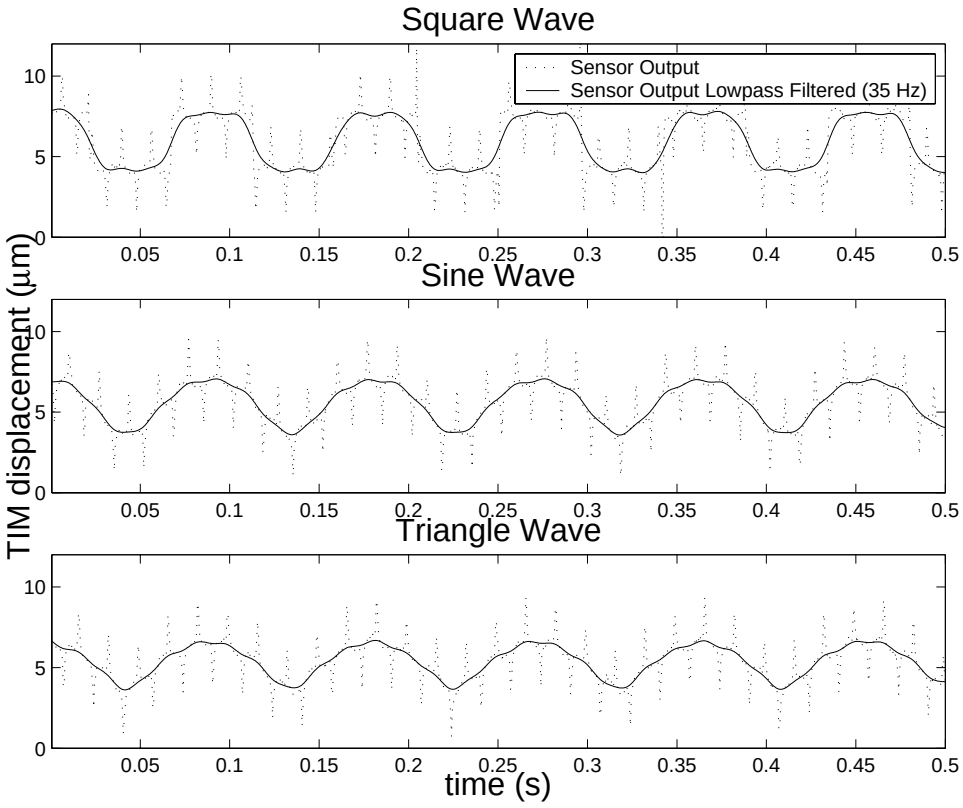

Figure 3.6: PMT output for various dynamic inputs to the TIM (open loop).

in identifying the source of the interference. Possible candidates for the source are interference between the two power supplies used, environmental noise, and unbalanced capacitance in the sensor design. As an interim solution, lowpass filtering the sensor output produces a usable signal although it severely limits the sensor bandwidth. Figure 3.6 shows the sensor output after it has been post processed by filtering forward and backward with a second-order Butterworth lowpass filter with a cutoff frequency of 35 Hz.

3.3 Control Design

Description of a Linear Low-Order Model for the TIM

A linear low-order model of TIM operation was developed to facilitate control design. A linear low-order model is useful in the early phases of system design and in designing feedback control laws.

To create our linear low-order model a pair of TIM beams is lumped into three control volumes: the shuttle and the two beams, one on each side of the shuttle. The heat that is generated and stored in each control volume is calculated as well as the heat transfer to adjacent control volumes, the anchor pads, and the substrate. The anchor pads and substrate are assumed to remain at room temperature. A schematic of the model is shown in Figure 3.7 and the resulting system of ordinary differential equations is listed in Equation 3.1.

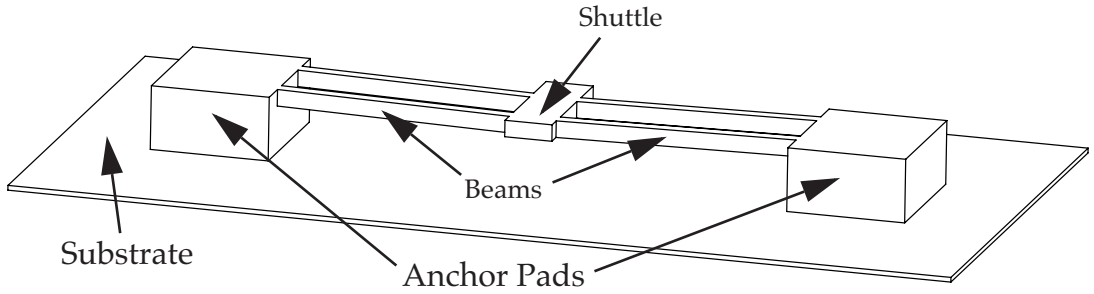

Figure 3.7: Schematic describing how the TIM was lumped into control volumes to create the linear low-order model.

$$\frac{dT_{b1}}{dt} = \frac{1}{C_b}\left[-\left(\frac{1}{R_{bp}} + \frac{1}{R_{bs}} + \frac{1}{R_{bw}}\right)T_{b1} + \frac{1}{R_{bs}}T_s + q\right]$$
$$\frac{dT_{b2}}{dt} = \frac{1}{C_b}\left[-\left(\frac{1}{R_{bp}} + \frac{1}{R_{bs}} + \frac{1}{R_{bw}}\right)T_{b2} + \frac{1}{R_{bs}}T_s + q\right] \qquad \text{Eq. 3.1}$$
$$\frac{dT_s}{dt} = \frac{1}{C_s}\left[\frac{1}{R_{bs}}T_{b1} + \frac{1}{R_{bs}}T_{b2} - \left(\frac{2}{R_{bs}} + \frac{1}{R_{sw}}\right)T_s\right]$$

T_{b1} and T_{b2} are the temperatures of the beams, T_s is the temperature of the shuttle, C_b and C_s are the heat capacities of the beams and the shuttle, R_{bp} is the thermal resistance between the beams and bond pads, R_{bs} is the thermal resistance between the beams and the shuttle, R_{bw} is the thermal resistance between the beams and the substrate, R_{sw} is the thermal resistance between the shuttle and the substrate, and q is the ohmic heat generation in the beams. The physical properties and dimensions used to define the above parameters are listed in Table 3.1. The equations used to define the parameters follow.

Table 3.1: Linear Low-Order Model Parameters

Parameter	Symbol	Value
thermal conductivity of polysilicon	k_s	32 W/m/K
thermal conductivity of air	k_a	0.026 W/m/K
out-of-plane thickness of the control volume	t	3.5 μm
distance between the control volumes and the substrate	g	2 μm
in-plane thickness of the beams	w_b	3 μm
in-plane thickness of the shuttle	w_s	12 μm
length of the beams	l_b	250 μm
length of the shuttle	l_s	15 μm
density of polysilicon	ρ	2330 kg/m^3
specific heat of polysilicon	c_p	705 J/kg/K
electrical resistivity of polysilicon	r_0	34 $\mu\Omega$m

The thermal resistance between adjacent control volumes and between control volumes and anchor pads was defined in the usual way and is shown in Equation 3.2.

$$\begin{aligned} R_{bp} &= \frac{l_b}{2k_s w_b t} \\ R_{bs} &= R_{bp} \\ R_{bw} &= \frac{g}{k_a w_b l_b S_b} \\ R_{sw} &= \frac{g}{k_a w_s l_s S_s} \end{aligned} \qquad \text{Eq. 3.2}$$

The thermal resistance between the control volumes and the substrate were modeled using a shape factor that approximates the effect of the heat transferring from the sides and bottoms of the control volumes to their effective projected area on the substrate [17]. The shape factors S_b and S_s are defined in Equation 3.3.

$$S_{(b/s)} = \frac{t}{w_{(b/s)}}\left(\frac{2g}{t} + 1\right) + 1 \qquad \text{Eq. 3.3}$$

The heat capacity of the control volumes is defined in Equation 3.4

$$C_{(b/s)} = w_{(b/s)} l_{(b/s)} t \rho c_p \qquad \text{Eq. 3.4}$$

The ohmic heat generation in the control volumes is accurately modeled as a quadratic function of the current—which can be found from the voltage applied to the TIM and the calculated resistance of the TIM—as shown in Equation 3.5 with V as the input voltage.

$$\begin{aligned} q &= \frac{I^2 r_b}{C_b} \\ &\text{where} \\ I &= \frac{V}{2r_b + r_s} \\ r_{(b/s)} &= \frac{r_0 l_{(b/s)}}{w_{(b/s)} t} \end{aligned} \qquad \text{Eq. 3.5}$$

To linearize the heat generation model a series of data points for the heat generated given various voltage inputs were fit to a line going through the origin

using a min-norm technique. A scaling factor of heat generation to voltage input of 452,280 K/s/V was determined from the linearization. Figure 3.8 shows a comparison of the quadratic and linear models.

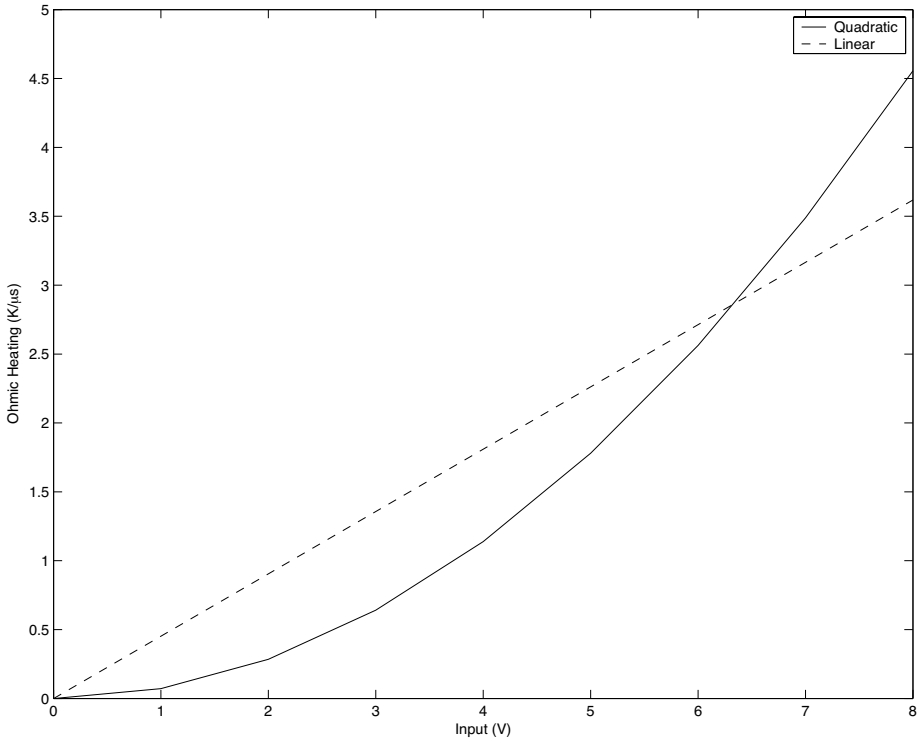

Figure 3.8: Comparison of quadratic and linearized ohmic heat generation functions.

From the system of ordinary differential equations (Equation 3.1) the temperature of the control volumes can be solved for as functions of time. By estimating the thermal expansion of the expansion beams an accurate prediction of the displacement of the TIM can be made using a Pseudo-Rigid-Body-Model [6] developed by Chris Lott [12]. Unfortunately it is also nonlinear. The displacement model is linearized as a scaling factor in a similar manner to the ohmic heating model using a series of displacements corresponding to average beam temperatures. A comparison of the nonlinear and linear models is found in Figure 3.9.

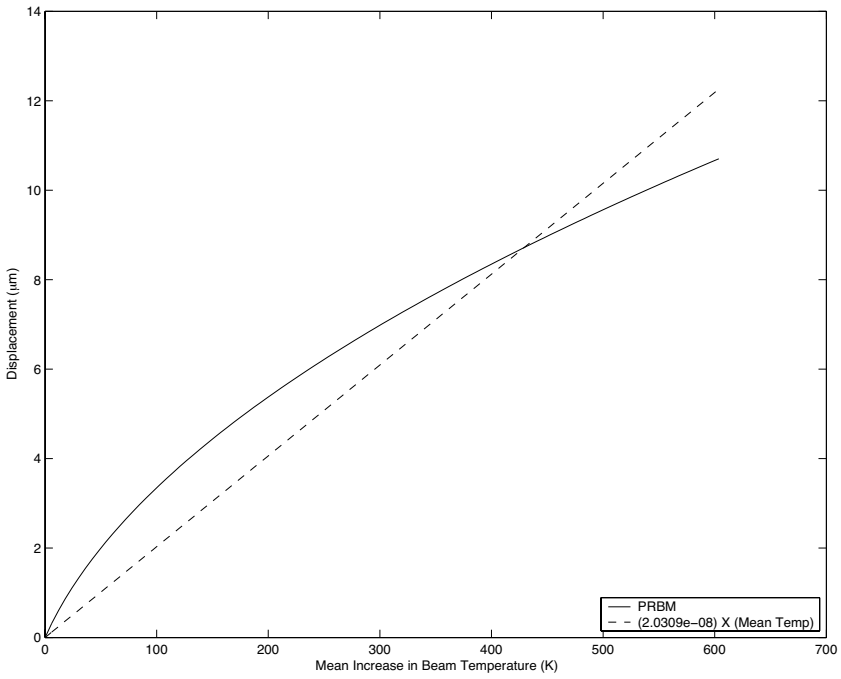

Figure 3.9: Comparison of the Pseudo-Rigid-Body-Model for the TIM and a linearization of that model.

To evaluate the accuracy of the linear low-order model just described it was compared with the nonlinear, three-dimensional, finite-element model described in Chapter 2. Both models were used to simulate the response of a TIM to a step input of 12 Volts, and a comparison of the results is in Figure 3.10. The linear low-order model provides predictions in the right range as it predicts the steady state response to within approximately five percent.

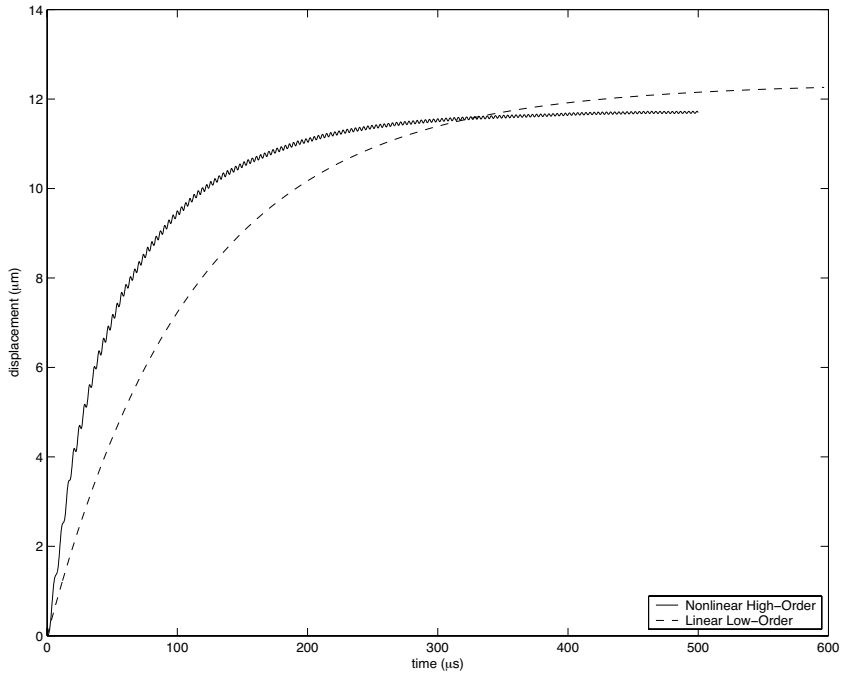

Figure 3.10: Comparison of the linear low-order model to a nonlinear FEA model.

3.4 Feedback Control of the TIM using the PMT

Proportional Control

In its simplest form feedback control is accomplished by producing an error signal that is the difference between a reference input, corresponding to a desired output, and the sensor signal monitoring the system output it is desired to control. This error signal is used as the input for a controller which produces a control signal to the system so that the error will converge to zero. In our case the sensor is a PMT monitoring the output displacement of a TIM, and the reference input is a voltage that corresponds to the PMT output for the desired TIM displacement.

Proportional control is a simple control law that can be used in which the output of the controller is a scalar multiple of the error signal. Unfortunately, controlling the TIM with proportional control will result in a steady-state error. This steady-state error is due to the fact that the TIM requires a non-zero voltage

input to increase the expansion leg temperature and therefore hold the shuttle any non-zero steady-state displacement. If the sensor output matches the reference input exactly then the error signal, and consequently the controller output, will be zero. What actually happens is the error signal converges to a finite value with the TIM at a steady-state displacement. Figure 3.11 shows the simulated unit step response for proportional control of the TIM. As shown the steady-state response of the systems is less than the unit reference input. The steady-state error can be reduced by increasing the proportional gain, but it only asymptotically approaches zero.

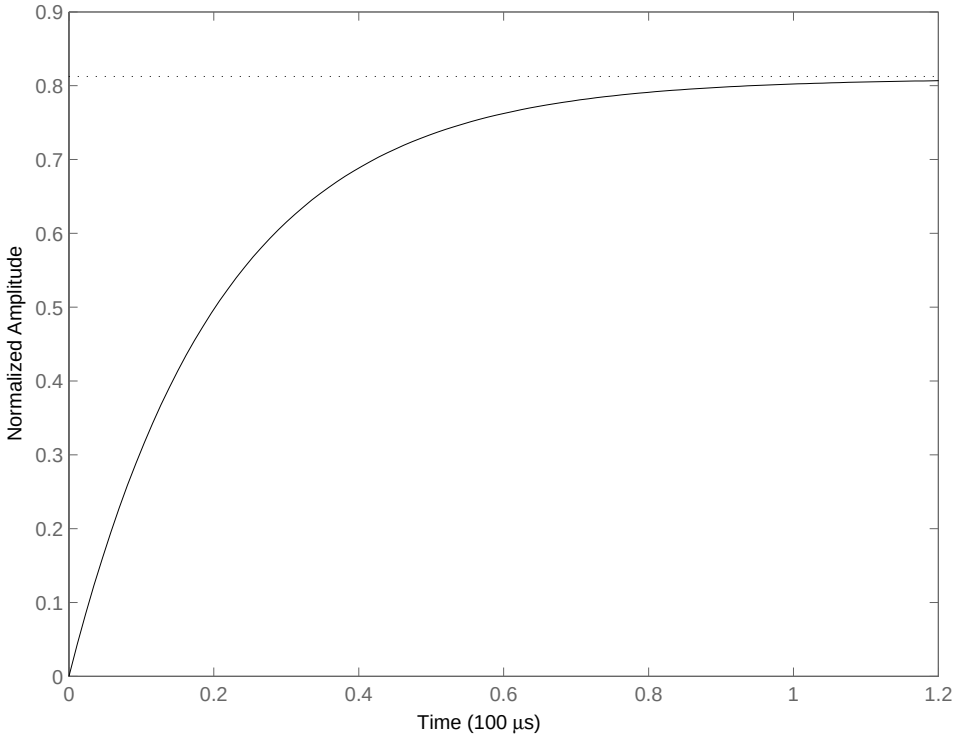

Figure 3.11: Simulated unit step response for proportional control of the TIM.

Proportional/Integral Control

To counteract this steady-state error problem, a proportional-integral control was used. In this case proportional control is augmented with an integrator that sums the error over time. This allows a zero error to produce a finite control

effort. Equation 3.6 is an analytical expression describing proportional-integral control with k_p and k_i the proportional and integral gains.

$$V_{control} = k_p V_{error} + k_i \int V_{error} dt \qquad \text{Eq. 3.6}$$

Figure 3.12 shows the simulated unit step response for proportional/integral control of the TIM. As can be seen, the system displaces to the proportional steady-state response, then the steady-state error is summed over time by the integration part of the control adding to the control effort until there is zero steady-state error. The time scales of Figures 3.11 and 3.12 demonstrate the sacrifice expected with proportional/integral control. In general, response time is increased when moving from proportional to proportional/integral control.

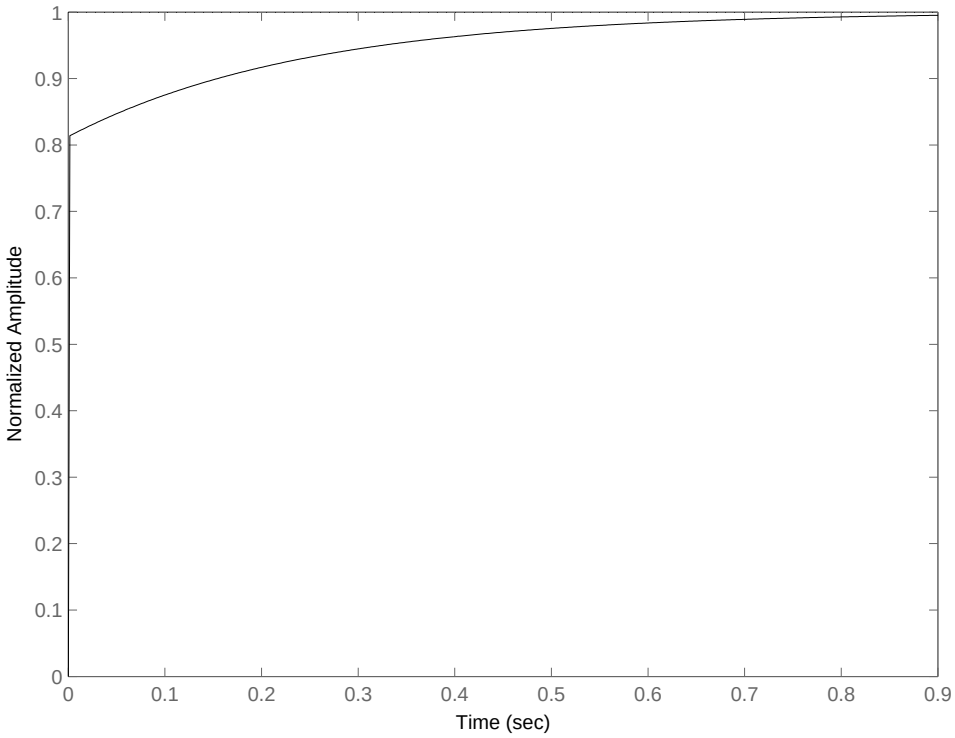

Figure 3.12: Simulated unit step response for proportional/integral control of the TIM.

3.5 Proportional/Integral Controller Implementation

A schematic showing the implementation of proportional/integral control of a TIM using PMT feedback sensing is in Figure 3.13. To provide a useful signal out of the PMT the voltage difference between points *a* and *b* on the bridge is mea-

sured using an op-amp set up as a differencing circuit. The resulting signal is shifted up and down with a DC offset to calibrate the signal for any zero offset. The shifted signal is amplified into a range that is easy to generate a reference input. The error signal is produced by using another differencing circuit that subtracts the amplified sensor output from the error signal. The error signal is input into the controller, which is implemented with an op-amp. The controller provides a signal to an amplifier that outputs a voltage equal to the controller signal, but provides enough current to drive the TIM.

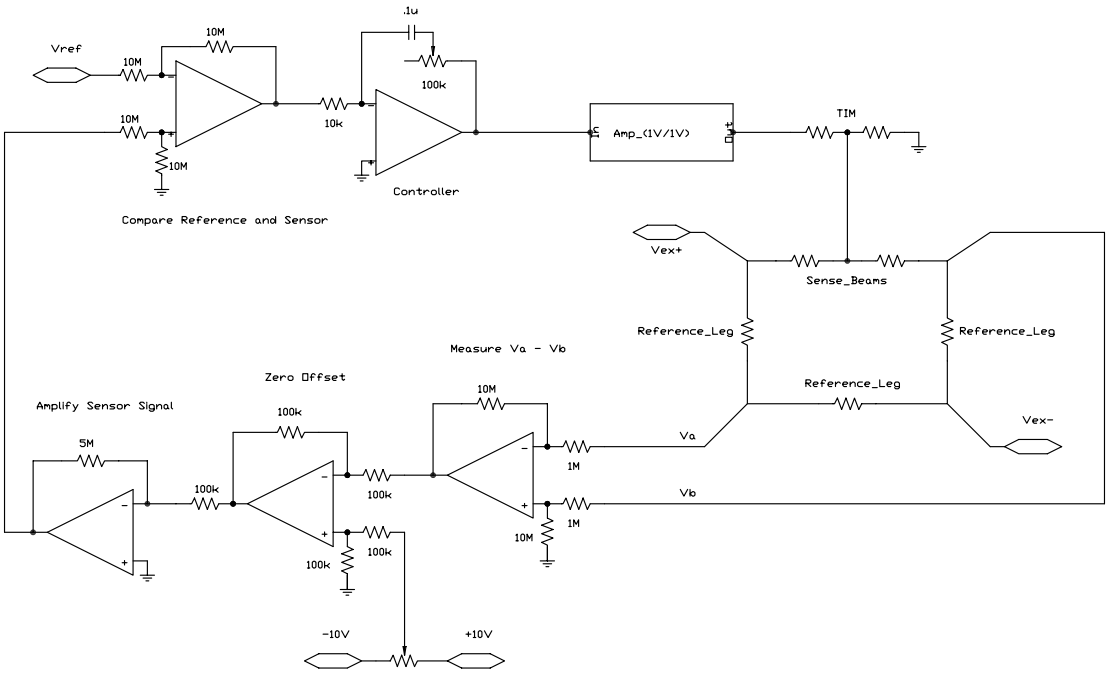

Figure 3.13: An electrical schematic illustrating the implementation of proportional-integral feedback control of a TIM using a PMT.

With feedback control implemented the system was driven with sine, square, and triangle waves at 11 Hz. The amplitude of the input signal matched the desired, amplified signal output. A comparison of the reference input signals and the resulting sensor outputs is in Figure 3.14. A post processed lowpass filter is used once again to aid in visualization. As shown in the plot, proportional/integral feedback control was successful in getting the sensor output to closely track the reference input.

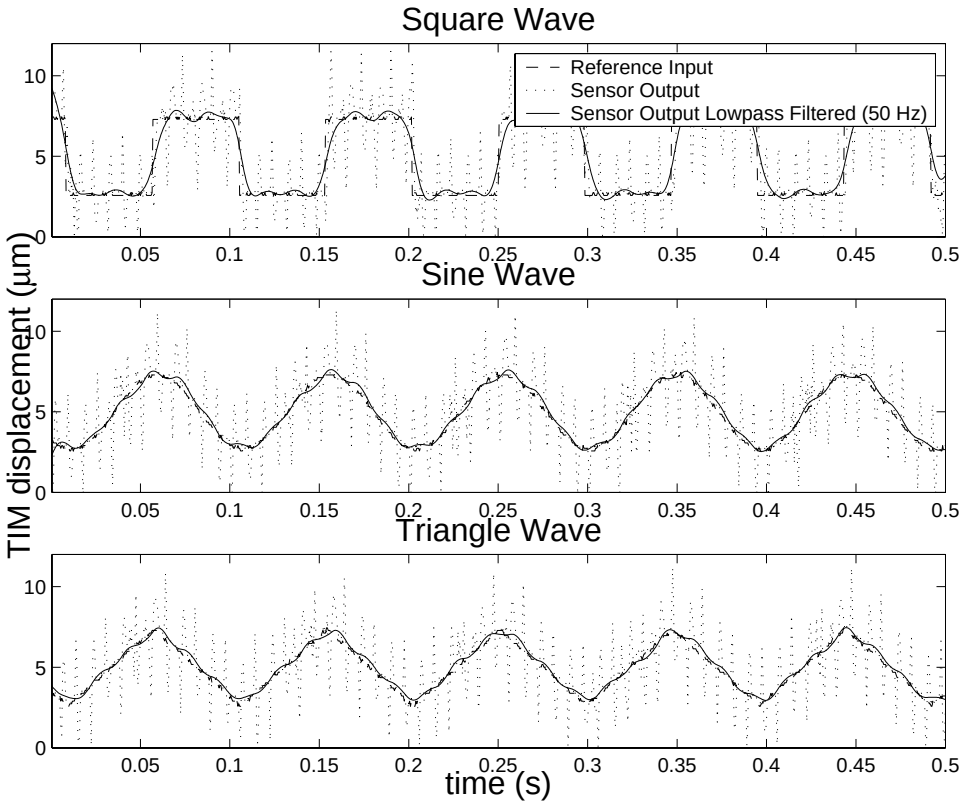

Figure 3.14: PMT output and reference input for a TIM with proportional/integral feedback control.

Unfortunately the noisy PMT signal corrupts the error signal that is input to the controller. The controller in turn provides a noisy control effort to the TIM. To determine how variable the TIM displacement is when driven by this noisy control effort, we measured the displacement when a constant reference input is applied. We took 100 samples at 30 samples/second using video capture on an optical microscope. While this is well below the Nyquist frequency of the interference and is therefore not sufficient to provide an accurate time history, it is sufficient to quantify the variability of the displacement. As can be seen from a histogram of the samples in Figure 3.15 the displacement varies by approximately 1.5 μm. This confirms that the sensor interference is actually noise and not a true indication of TIM displacement as the sensor indicates approximately 8 μm of variation.

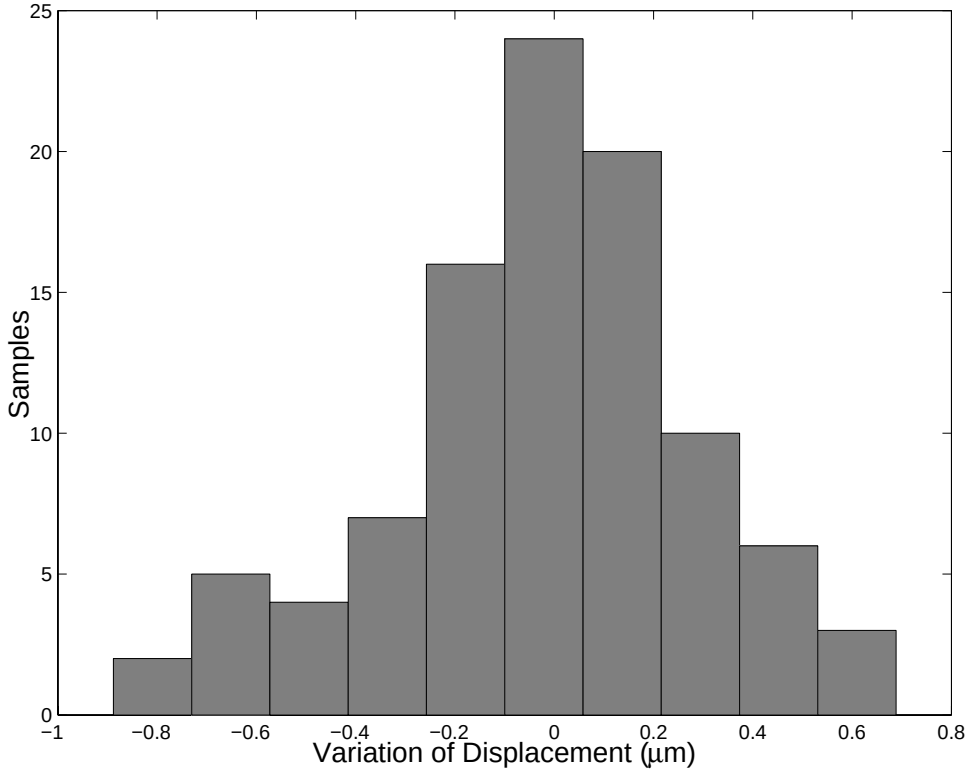

Figure 3.15: Histogram of Proportional/Integral controlled TIM with a constant reference input.

As suggested in an earlier section a solution for minimizing the interference is to apply a lowpass filter to the sensor output. While this limits the system bandwidth it provides for more accurate control at low driving frequencies. Given that the current performance of the sensor is limited by the interference to less than 70 Hz, it is not a significant loss to reduce the bandwidth further. If the sensor bandwidth could be extended past the time constant of the TIM at approximately 25 kHz we could use feedback control to reduce the response time of the system. Figure 3.16 shows the effect of applying a second-order Butterworth lowpass filter to the sensor output. As expected, the effect on system performance is better reference input tracking at low frequencies.

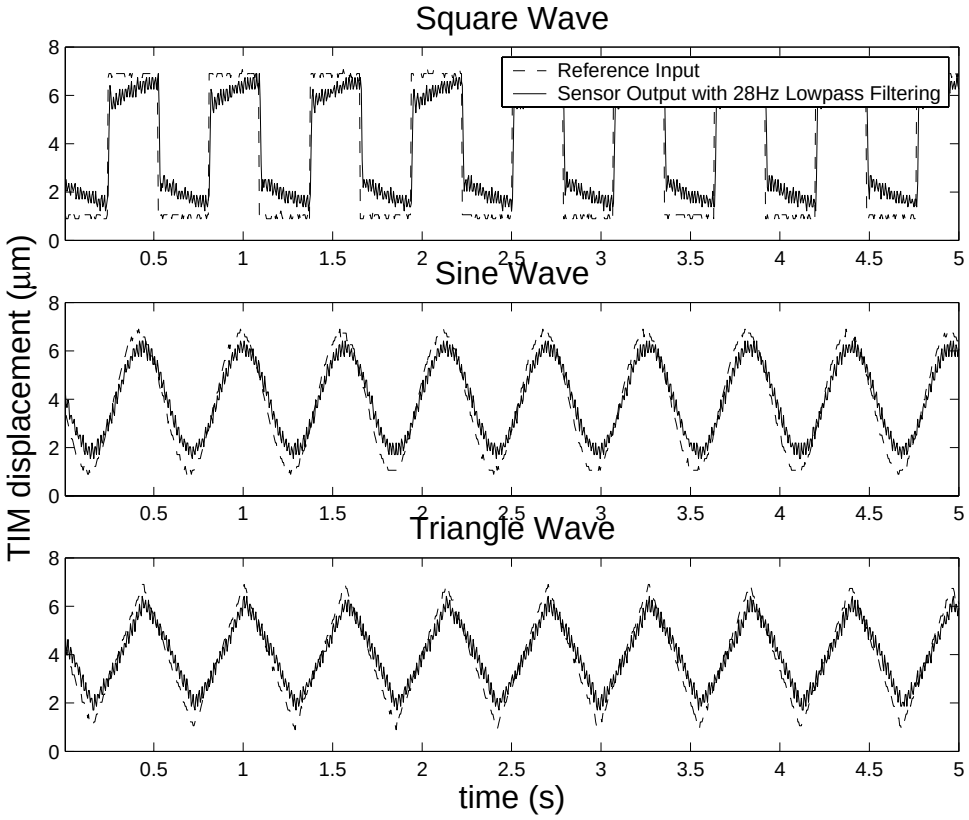

Figure 3.16: PMT output and reference input for a TIM with proportional/ integral feedback control and lowpass filtering.

Results from the square wave input clearly show the effect of the integrator as the steady-state error is gradually eliminated after each step. This response is similar to the simulated response shown in Figure 3.12. Results from the sine wave input show the bandwidth limiting effects of the lowpass filter as the output magnitude is a little less than the input. The input sine wave has a frequency of 1.8 Hz which is about one decade lower than the lowpass filter cutoff frequency of 28 Hz. One decade lower than the cutoff is where we expect to begin seeing effects on the output magnitude.

3.6 Conclusions

Through the candidate application of implementing feedback control on a TIM using the PMT, it is shown that piezoresistive sensing is effective at monitoring the real-time operation of polysilicon micro-devices. Being able to monitor

the current conditions of a micro-scale system allows for more robust and accurate operation as is also shown with our candidate application. A sensor that is on the same spacial scale, and is manufactured on chip using the same fabrication steps used to make the micro-scale system will have a much greater chance of being implemented in a broad range of applications than do large, expensive sensors such as laser Doppler vibrometers or scanning electron microscopes. Piezoresistive on-chip sensing in particular has the additional advantages of using simple analog circuitry and of possibly being integrated directly into the devices it is desired to monitor.

Through the use of a simplified linear model effective Proportional/Integral feedback control has been designed and tested for a surface micromachined thermal actuator. Additionally, with the application of lowpass filtering the PMT has proven capable for implementing feedback control on the actuator for low bandwidth purposes. It is anticipated that identifying and eliminating the source of the sensor interference will allow us to increase the closed-loop bandwidth of the system to frequencies in the 100 kHz range. This will enable significant improvements in thermal actuator response time.

CHAPTER 4 CONCLUSIONS AND RECOMMENDATIONS

4.1 Conclusions

Modeling Thermal Microactuators

Surface micromachined thermal actuators have proven useful for actuating a variety of compliant MEMS devices. As such, significant work has been done in the field of modeling thermal actuators. This research has built upon previously accomplished work by incorporating all of the physical phenomena found to be significant into a sophisticated high-order model. The high-order model includes the affects of temperature-dependent material properties and large-deformation nonlinearities demonstrated by others to be significant. This enables the model to predict steady-state response to within one percent of measured response. Additionally this high-order model calculates solution in all three dimensions. Lower dimensional modeling requires the assumption of a fully developed temperature profile in the air between the actuator and the substrate. Modeling all three dimensions provides for accurate prediction throughout the entire transient response and not just at steady-state.

High speed video data of thermal actuator transient responses was taken and analyzed for model validation. By measuring the actuator response throughout its transient it has been shown that there are undescribed factors slowing the

actuator response. This is unobservable when only measuring the steady-state response.

The result is an experimentally validated three-dimensional multi-physics nonlinear transient finite element model for thermal actuators. The usefulness of the model has been demonstrated by examining a technique involving the use of short pulses to actuate thermal actuators. It was predicted and experimentally validated that actuating with short pulses is effective at reducing response time and energy consumption.

Piezoresistive Sensing of MEMS Devices

The capability of piezoresistive feedback sensing in MEMS devices has been demonstrated by physically implementing proportional/integral feedback control on the displacement of a TIM. The piezoresistive sensor provided a consistent and usable output voltage to infer TIM displacement. It also exhibited an acceptable signal-to-noise ratio enabling off-chip control circuitry. Piezoresistive feedback sensing of MEMS devices promises an economical method for significantly improving the reliability and performance of MEMS devices.

Secondarily it has been shown that the TIM can be effectively controlled using proportional/integral feedback control. This has been demonstrated both with a simple lumped and linearized model as well as with the physical control implementation.

4.2 Recommendations

Modeling Thermal Microactuators

Although the high-order model developed in this research provides a useful lower bound for thermal actuator response time it is desirable to improve prediction accuracy. To improve the accuracy of transient response predictions, it is recommended that further studies be performed to quantify the sources and effects of friction in the micro environment. For example, by incorporating a friction model in the high-order model it may be possible to validate that friction is the main factor causing discrepancies between predicted and measured response

time of thermal actuators as well as provide an estimate quantification of that friction.

Piezoresistive Sensing of MEMS Devices

While the implementation of piezoresistive sensing was successful, it did reveal some challenges that remain in fully developing the technology. Of particular note is the periodic interference spikes which significantly reduce the sensor bandwidth. Identifying and eliminating the source of the interference will greatly improve the utility of the sensor.

Piezoresistive sensing also shows great promise for monitoring other surface micromachined devices, and it is recommended that further implementation of piezoresistive sensing be implemented. One elegant aspect of piezoresistive sensing that should be pursued is the ability to incorporate the sensor into the device being sensed. For example one potential application is a micro sized nanopositioner in which thermal actuators position a multiple-degree-of-freedom moveable stage to accuracies measured in nanometers. The piezoresistive feedback sensor could be incorporated into the actuators or the stage.

Another example is in non-contact force threshold detectors. In this example a compliant bistable mechanism is fabricated so that it switches between its bistable states when a sufficient force is applied. Due to the piezoresistive effect the resistance across the bistable mechanism will be different for its two different stable positions. Using the change in resistivity of the compliant members as an indication of the strain, it should be possible to determine the state of the device. By designing the device to switch states when it experiences a certain level of force, these devices could be used to detect when a certain force threshold has been exceeded. The force could be inertial, magnetic, or the output of a thermal actuator for example.

These devices could be implemented in an array with each device having a different threshold to enable the detection of the peak force level that the device has experienced. Ideally, these devices would be packaged so that they could be easily queried to determine the state of the threshold detector. Potential applica-

tions include shock force detection on shipping containers, impact switches, and inexpensive remote seismic sensors.

Because they can maintain their state in the event of a power loss, bistable microswitches could be useful for developing nonvolatile mechanical memory arrays where high data security is essential. One challenge in the design of microswitches is the integrity of the contact and the need to maintain a contact force. In the case of mechanical memory, where the switch does not transmit any power, the need to maintain contact is not essential provided there is some means to sense the state of the switch. The piezoresistive properties of polysilicon allow the state of a bistable switch to be sensed directly without the need for contacts. A broad field of possible MEMS applications has been opened that take advantage of the piezoresistive property of polysilicon.

REFERENCES

[1] Maluf, N., 2000, *An Introduction to Microelectromechanical Systems Engineering*, Artech House, Norwood, MA.

[2] Comtois, J.H., Bright, V. M., Phipps, M.W., 1995, "Thermal microactuators for surface-micromachining processes," *Proceedings of SPIE - The International Society for Optical Engineering*, v. 2642, p. 10-21.

[3] Cragun, R., 1998, "Constrained thermal expansion micro-actuator," *ASME, Dynamic Systems and Control Division (Publication) DSC, 66, Micro-Electro-Mechanical Systems (MEMS)*, p. 365-371.

[4] Que, L., Otradovec, A.D., Gianchandani, Y.B., 2001, "Pulse and DC operation lifetimes of bent-beam electrothermal actuators," *Proceedings of the IEEE Micro Electro Mechanical Systems (MEMS)*, p. 570-573.

[5] Legtenberg, R., Groeneveld, A.W., Elwenspoek, M., 1996, "Comb-drive actuators for large displacements," *Journal of Micromechanics and Microengineering*, v. 6, n. 3, p. 320-329.

[6] Howell, L.L., 2001, *Compliant Mechanisms*, Wiley, New York, New York.

[7] Maboudian, R., Howe, R.T., 1997, "Critical Review: Adhesion in surface micromachined structures," J. Vac. Sci. Technology B, v. 15, n. 1, p. 1-20.

[8] Baker, M.S., and Howell, L.L., 2002, "On-Chip Actuation of an In-Plane Compliant Bistable Micro-Mechanism," *Journal of Microelectromechanical Systems*, v. 11, n. 5, p. 566-573.

[9] Jensen, B.D., and Howell, L.L., "Identification of Compliant Pseudo-Rigid-Body Mechanism Configurations Resulting in Bistable Behavior," *Journal of Mechanical Design*, in press.

[10] Masters, N.D., and Howell, L.L., 2003, "A Self-Retracting Fully-Compliant Bistable Micromechanism," *Journal of Microelectromechanical Systems*, v. 12, n. 3, p. 273-280,.

[11] Lott, C., 2001, *Electrothermalmechanical Modeling of a Surface-micromachined Linear Displacement Microactuator*, MS Thesis, Brigham Young University.

[12] Lott, C., McLain, T.W., Harb, J.N., Howell, L.L., 2002, "Modeling the thermal behavior of a surface-micromachined linear-displacement thermomechanical microactuator," *Sensors and Actuators*, v. 101, n. 1-2, p. 239-250.

[13] Chiao, M., Lin, L., 1997, "Microactuators based on electrothermal expansion of clamped-clamped beams," *ASME, Dynamic Systems and Control Division (Publication) DSC, 62, Micro-Electro-Mechanical Systems (MEMS)*, p. 75-80.

[14] Que, L., Park, J.S., Gianchandani, Y.B., 2001, "Bent-beam electrothermal actuators-Part I: Single beam and cascaded devices," *Journal of Microelectromechanical Systems*, v. 10, n. 2, p. 247-254.

[15] Park, J.S., Chu, L.L., Siwapornsathain, E., Oliver, A.D., Gianchandani, Y.B., 2000, "Long throw and rotary output electro-thermal actuators based on bent-beam suspensions," *Proceedings of the IEEE Micro Electro Mechanical Systems*, p. 680-685.

[16] Hickey, R., Sameoto, D., Hubbard, T., Kujath, M., 2002, "Time and frequency response of two-arm micromachined thermal actuators," *Journal of Micromechanics and Microengineering*, v. 13, p. 40-46.

[17] Lin, L., Chiao, M., 1996, "Electrothermal responses of lineshape microstructures," *Sensors and Actuators A*, v. 55, p. 35-41.

[18] Horsley, D.A., Wongkomet, N., Horowitz, R., and Pisano, A.P., 1999, "Precision positioning using a microfabricated electrostatic actuator," IEEE Transactions on Magnetics, v. 35, p. 993-999.

[19] Smith, S.T., Chetwynd, D.G., Harb, S., 1994, "A simple two-axis ultraprecision actuator," *Review of Scientific Instruments*, v. 65, pp. 910-917.

[20] Hasegawa, T., Majima, S., 1998, "Control system to compensate the hysteresis by Preisach model on SMA actuator," *Proceedings of the 1998 9th International Symposium on Micromechatronics and Human Science*, p. 171-176.

[21] Lyshevski, S.E., 2001, "Nonlinear microelectromechanical systems (MEMS) analysis and design via the Lyapunov stability theory," *Proceedings of the IEEE Conference on Decision and Control*, v. 5, p. 4681-4686

[22] Hernandez, D., Park, S.S., Horowitz, R., Packard, A.K., 1999, "Dual-stage track following servo design for hard disk drives," *Proceedings of the American Control Conference*, v. 6, p. 953-958.

[23] Hirano, T. Fan, L.S., Lee, W.Y., Hong, J., Imaino, W., Pattanaik, S., Chan, S., Webb, P., Horowitz, R., Aggarwal, S., Horsley, D.A., 1998, "High-bandwidth high-accuracy rotary microactuators for magnetic hard disk drive tracking servos," *IEEE/ASME Transactions on Mechatronics*, v. 3, n. 3, p. 156-165.

[24] Horsley, D.A., Horowitz, R., Pisano, A.P., 1998, "Microfabricated electrostatic actuators for had disk drives," *IEEE/ASME Transactions on Mechatronics*, v. 3, n. 3, p. 175-183.

[25] Lee, S.H., Baek, S.E., Kin, Y.H., 2000, "Design of a dual-stage actuator control system with discrete-time sliding mode for hard disk drives," *Proceedings of the IEEE Conference on Decision and Control*, v. 4., p. 3120-3125.

[26] Li, Y., Horowitz, R., 2000, "Track-following controller design of MEMS based dual-stage servos in magnetic hard disk drives," *Proceedings - IEEE Conference on Robotics and Automation*, v. 1, p. 953-958.

[27] Semba, T., Hirano, T., Hong, J., Fan, L.S., 1999, "Dual-stage servo controller for HDD using MEMS microactuator," *IEEE Transactions on Magnetics*, v. 35, n. 5, pt. 1, p. 2271-2273.

[28] Sun, Y., Piyabongkam, K., Sezen, A., Nelson, B.J., Rajamani, R., Schoch, R., Potasek, D.P., 2002, "A novel dual-axis electrostatic microactuation system for micromanipulation," *IEEE International Conference on Intelligent Robots and Systems*, v. 2, p. 1796-1801.

[29] Schellin, R., Hess, G., 1992, "Silicon subminiature microphone based on piezoresistive polysilicon strain gauges," *Sensors and Actuators*, v. 32, n. 1-3, p. 555-559.

[30] Liang, Y., Kenny, T., 1998, "Mechanical optimization of a dual-axis piezoresistive force sensor," *ASME, DSC Division, MEMS*, v. 66, p. 389-394.

[31] Joseph, H., Swafford, B., Terry, S., 1997, "MEMS in the medical world," *Sensors*, v. 14, n. 4, p. 47-51.

[32] Koester, D.A., Mahadevan, R., Hardy, B., and Markus, K.W., 2000, MUMPs Design Handbook, Rev. 5.0, Cronos Integrated Microsystems, http://www.memsrus.com.

[33] Maginell, R.P., 1997, "Polycrystalline-Silicon Microbridge Combustible Gas Sensor," *Ph.D. Dissertation*, University of New Mexico.

[34] Barin, I., 1993, *Thermochemical Data of Pure Substances*, VCH, Weinheim.

[35] Okada, Y., Tokumaru, Y., 1984, "Precise determination of lattice parameter and thermal expansion coefficient of silicon between 300 and 1500 K," *Journal of Applied Physics*, v. 56, n. 2, p. 314-320.

[36] Incropera, F.P., DeWitt, D.P., 1996, *Fundamentals of Heat and Mass Transfer*, 4th Ed., John Wiley & Sons, New York.

[37] Tai, Y.C., Mastrangelo, C.H., Muller, R.S., 1988, "Thermal conductivity of heavily doped low-pressure chemical vapor deposited polycrystalline silicon films," *Journal of Applied Physics*, v. 63, n. 5, p. 1442-1447.

APPENDIX A

Table A.1: Values and Temperature Dependencies for Material Properties of Polysilicon. Temperatures in K.

Material Property	Values	Units	Refs.
Thermal Conductivity (k)	$k = (-6.8964 \times 10^{-10})T^4 + (2.0236 \times 10^{-6})T^3 + (-0.0021)T^2 + (0.8912)T + (-36.225))$	$\frac{W}{mK}$	[33]
Specific Heat (C_p)	$C_p = (-2.5167 \times 10^{-10})T^4 + (1.1412 \times 10^{-6})T^3 + (-0.0019)T^2 + (1.5504)T + 402.7723$	$\frac{J}{kgK}$	[33,34]
Density (ρ)	$\rho = 2330$	$\frac{kg}{m^3}$	—
Thermal Expansion (α)	$\alpha(T) = (-3.3802 \times 10^{-18})T^4 + (1.474 \times 10^{-14})T^3 + (-2.3857 \times 10^{-11})T^2 + (1.7105 \times 10^{-8})T + (-9.1455 \times 10^{-7})$	–	[35]

Table A.1: (Continued) Values and Temperature Dependencies for Material Properties of Polysilicon. Temperatures in K.

Material Property	Values	Units	Refs.
Resistivity	$\rho(T) = (20 \times 10^{-6}) \times [1 + (1.7 \times 10^{-3})(T - T_o)]$	Ωm	—[a]

a. From measurement of SUMMiT V“ process runs taken at Sandia National Laboratory.

Table A.2: Values and Temperature Dependencies for Material Properties of Air. Temperatures in K.

Material Property	Values	Units	Reference
Thermal Conductivity (k)	$k(T)$ input directly from a published table	$\frac{W}{mK}$	[36]
Specific Heat (C_p)	$C_p(T)$ input directly from a published table	$\frac{J}{kgK}$	[36]
Density (ρ)	$\rho(T)$ input directly from a published table	$\frac{kg}{m^3}$	[36]

Table A.3: Values and Temperature Dependencies for Material Properties of the Silicon Substrate. Temperatures in K.

Material Property	Values	Units	Reference
Thermal Conductivity (k)	$k = 32$	$\frac{W}{mK}$	[37]
Specific Heat (C_p)	$C_p = 705$	$\frac{J}{kgK}$	[34]
Density (ρ)	$\rho = 2330$	$\frac{kg}{m^3}$	—

APPENDIX B

```
/BATCH
/filename,thermal
/config,nres,1000000


!==================== Simulation Parameters ====================

!length of simulation from input voltage file
tf = 500e-6
!number of time steps from input voltage file
tn = 1204
!number of of temperature profile substeps to be read into structural simulation
ln = 100
!minimum and maximum time step for iterative solver
tmin = 1e-7
tmax = 1e-5

!read in input voltage vs time file (*tread,inputvolt,[filename],[extention],[direc-
        tory])
*dim,inputvolt,table,tn,1,,time
```

```
*tread,inputvolt,ta2_1voltages,txt
!inputvolt = 10


!==================== Define Geometry ====================

!Linear Dimensions in Microns

!Number of Leg Pairs
nl = 4

!Out of Plane Heighth of legs and shuttle
h = 2.52
!Gap Between Legs and Substrait
g = 2.04
!Gap Between Legs
gl = 2.8
!Leg inclination Offset (Microns)
O = 4.833
!Length of Leg
Ll = 248
!Width of Leg
Wl = 2.04

!Length of Shuttle if only 1 leg pair else program determined
Ls = 30
!Width of Shuttle (Orthogonal to Movement)
Ws = 17

!Width of Pad (Orthogonal to Movement)
Wp = 100
```

```
!Length of Pad (Direction of Movement)
Lp = Ls

!Width of wafer (Orthogonal to Movement)
Ww = 2*Wp+2*Ll+Ws+500
!Length of wafer (Direction of Movement)
!Lw = (nl)*(wl+gl)+50
Lw = 800
!Thickness of wafer
Tw = 50

!Width of Air
Wa = Ww
!Length of Air
La = Lw
!Thicness of Air
Ta = 50


!========== Define Material Properties (Units) ==========

!Youngs Modulus of PolySi (kg/s^2/micron)
modsi = 169e3

!Poissons Ratio of PolySi (Dimensionless)
poisson = .22

!Thermal Expansion of PolySi (1/K^n)
thermx = 2.7e-6
thermx0 = -9.1455e-7
thermx1 = 1.7105e-8
```

thermx2 = -2.3857e-11

thermx3 = 1.4740e-14

thermx4 = -3.3802e-18

!Thermal Conductivity of PosySi (kg*micron/s^3/CK^n)

k = 32e6

k0 = -36.225e6

k1 = .8312e6

k2 = -.0021e6

k3 = 2.0236

k4 = -6.8964e-4

!Initial Temperature/Environmental Temperature (K)

T0 = 300

!Specific Heat of Polysi (micron^2/s^2/K^n)

C = 705e12

C0 = 402.7723e12

C1 = 1.5504e12

C2 = -.0019e12

C3 = 1.1412e6

C4 = -2.5162e2

!Resistivity of PolySi (Ohm*micron)

ro = 2.0e-11

chsi = 1.7e-3 !(1/K)

!Density of PolySi (kg/micron^3)

density = 2330e-18

!Thermal Conductivity of MonoSi

kw = 32e6

!Specific Heat of Monosi
Cw = 705e12

!Density of MonoSi
!same at for PolySi

!Thermal Conductivity of Air (kg*micron/s^3/K^n)
kair = 26e3
kair0 = 3.9539e2
kair1 = 98.86
kair2 = -4.367e-2
kair3 = 1.301e-5

!Specific Heat of Air at Temp intervals of 100K from 300K to 1500K (micron^2/s^2/K)
c0air = 1.01e15
c0air300 = 1.007e15
c0air400 = 1.014e15
c0air500 = 1.03e15
c0air600 = 1.051e15
c0air700 = 1.075e15
c0air800 = 1.099e15
c0air900 = 1.121e15
c0air1000 = 1.141e15
c0air1100 = 1.159e15
c0air1200 = 1.175e15
c0air1300 = 1.189e15
c0air1400 = 1.207e15
c0air1500 = 1.248e15

```
!Density of Air at Temp intervals of 100K from 300K to 1500K (kg/micron^3)
desityair = 1e-18
densityair300 = 1.1614e-18
densityair400 = .8711e-18
densityair500 = .6964e-18
densityair600 = .5804e-18
densityair700 = .4975e-18
densityair800 = .4354e-18
densityair900 = .3868e-18
densityair1000 = .3482e-18
densityair1100 = .3166e-18
densityair1200 = .2902e-18
densityair1300 = .2679e-18
densityair1400 = .2488e-18
densityair1500 = .2322e-18


!**** Preprocessor ****
/PREP7


!========== Define Element Types ==========

!Tetrahedral Coupled-Field Solid
et,1,solid98,1

!Tetrahedral Thermal Solid
et,2,solid87
```

```
!========== Create Material Types for thermal analysis ==========

mp,dens,1,density
mptemp,1,T0,3000
mp,rsvx,1,ro*(1-chsi*T0),ro*chsi
!mp,rsvx,1,ro
mptemp
mptgen,1,51,300,10
mp,kxx,1,k0,k1,k2,k3,k4
!mp,kxx,1,k
mptemp
mptgen,1,100,300,12
mp,C,1,C0,C1,C2,C3,C4
!mp,C,1,C

!MonoSi (Mat #2)
mptemp
mp,dens,2,density
mp,kxx,2,kw
mp,C,2,Cw

!Air (Mat #3)
mptemp
mptgen,1,100,300,12
mp,kxx,3,kair0,kair1,kair2,kair3
!mp,kxx,3,kair
mptemp
mptgen,1,13,300,100
mpdata,C,3,1,c0air300,c0air400,c0air500,c0air600,c0air700,c0air800
mpdata,C,3,7,c0air900,c0air1000,c0air1100,c0air1200,c0air1300,c0air1400
mpdata,C,3,13,c0air1500
```

```
!mp,C,3,C0air
mpdata,dens,3,1,densityair300,densityair400,densityair500,densityair600,density
      air700,densityair800
mpdata,dens,3,7,densityair900,densityair1000,densityair1100,densityair1200,dens
      ityair1300,densityair1400
mpdata,dens,3,13,densityair1500
!mp,dens,3,densityair


!==================== Create Geometry ====================

!Left Leg
*do,nn,1,nl,1
k,(nn-1)*16+1,-Ws/2,-Wl/2+O/2+(nn-1)*(gl+nl),g
k,(nn-1)*16+2,-Ws/2,+Wl/2+O/2+(nn-1)*(gl+nl),g
k,(nn-1)*16+3,-Ws/2-Ll,+Wl/2-O/2+(nn-1)*(gl+nl),g
k,(nn-1)*16+4,-Ws/2-Ll,-Wl/2-O/2+(nn-1)*(gl+nl),g
k,(nn-1)*16+5,-Ws/2,-Wl/2+O/2+(nn-1)*(gl+nl),g+h
k,(nn-1)*16+6,-Ws/2,+Wl/2+O/2+(nn-1)*(gl+nl),g+h
k,(nn-1)*16+7,-Ws/2-Ll,+Wl/2-O/2+(nn-1)*(gl+nl),g+h
k,(nn-1)*16+8,-Ws/2-Ll,-Wl/2-O/2+(nn-1)*(gl+nl),g+h
v,(nn-1)*16+1,(nn-1)*16+2,(nn-1)*16+3,(nn-1)*16+4,(nn-1)*16+5,(nn-1)*16+6,(nn-
      1)*16+7,(nn-1)*16+8

!Right Leg
k,(nn-1)*16+9,Ws/2,-Wl/2+O/2+(nn-1)*(gl+nl),g
k,(nn-1)*16+10,Ws/2,+Wl/2+O/2+(nn-1)*(gl+nl),g
k,(nn-1)*16+11,Ws/2+Ll,+Wl/2-O/2+(nn-1)*(gl+nl),g
k,(nn-1)*16+12,Ws/2+Ll,-Wl/2-O/2+(nn-1)*(gl+nl),g
k,(nn-1)*16+13,Ws/2,-Wl/2+O/2+(nn-1)*(gl+nl),g+h
k,(nn-1)*16+14,Ws/2,+Wl/2+O/2+(nn-1)*(gl+nl),g+h
```

```
k,(nn-1)*16+15,Ws/2+Ll,+Wl/2-O/2+(nn-1)*(gl+nl),g+h
k,(nn-1)*16+16,Ws/2+Ll,-Wl/2-O/2+(nn-1)*(gl+nl),g+h
v,(nn-1)*16+9,(nn-1)*16+10,(nn-1)*16+11,(nn-1)*16+12,(nn-1)*16+13,(nn-
        1)*16+14,(nn-1)*16+15,(nn-1)*16+16
*enddo

*if,nl,eq,1,then
!Shuttle
BLOCK,-Ws/2,Ws/2,-Ls/2,Ls/2,g,g+h

!Anchor/Bond Pads
BLOCK,-Ws/2-Ll-Wp,-Ws/2-Ll,-Lp/2,Lp/2,0,g+h
BLOCK,Ws/2+Ll+Wp,Ws/2+Ll,-Lp/2,Lp/2,0,g+h

*else
!Shuttle
BLOCK,-Ws/2,Ws/2,-Wl/2+o/2,+Wl/2+O/2+(nl-1)*(gl+nl),g,g+h

!Anchor/Bond Pads
BLOCK,-Ws/2-Ll-Wp,-Ws/2-Ll,-Wl/2-o/2,+Wl/2-O/2+(nl-1)*(gl+nl),0,g+h
BLOCK,Ws/2+Ll+Wp,Ws/2+Ll,-Wl/2-o/2,+Wl/2-O/2+(nl-1)*(gl+nl),0,g+h
*endif

!Combine Geometry to Create Actuator
vadd,all
numcmp,volu
cm,actuator,volu
vatt,1,,1

!Wafer
BLOCk,-Ww/2,Ww/2,-Lw/2,Lw/2,-Tw,0
```

```
!Attach and name components
vglue,all
numcmp,volu
vsel,s,volu,,1
!cm,actuator,volu
vatt,1,,1

vsel,inve
cm,wafer,volu
vatt,2,,2

allsel,all
cm,si,volu

!Air
BLOCK,-Wa/2,Wa/2,-La/2,La/2,0,Ta
vsbv,3,si,,delete,keep
allsel,all
vglue,all
cmsel,s,si
vsel,inve
cm,air,volu
vatt,3,,2

allsel,all


!==================== Mesh ====================

!Mesh the Actuator
```

```
esize,5
mshape,0,3d
!smrtsize,8
vmesh,actuator
krefine,1,16,1,1,2

!Mesh the Wafer
esize,40
!smrtsize,10
vmesh,wafer

!Mesh the Air
vmesh,air



!========== Define Boundry Conditions for Thermal Analysis ==========

!Select Bottom Surface of Right Bond Pad
asel,s,loc,z,0
asel,r,loc,x,Ws/2+Ll,Ws/2+Ll+Wp

!Voltage
da,all,volt,0

!Select Botttom Surface of Wafer
asel,s,loc,z,-Tw

!Temperature
da,all,temp,T0

!Close Preprocessor
```

```
allsel,all
finish

!**** Solver ****
/solu


!==================== Initial Contions ====================

!Start at room temperature
tunif,T0
ic,all,temp


!==================== Solution Options ====================

!Solution Type (0=Steady State, 4=Transient)
antype,4
outres,all,all
!cnvtol,temp,,.01
!cnvtol,amps,,.5
neqit,20
!nsubst,6
!nropt,full,,on


!========== Define Load Steps for Thermal Problem ==========

!Select Bottom Surface of Left Bond Pad
asel,s,loc,z,0
asel,r,loc,x,-Ws/2-Ll,-Ws/2-Ll-Wp
```

```
!Write Load Step File
time,tf
deltim,tmin,tmin,tmax
autots,1
KBC,1
da,all,volt,%inputvolt%
lswrite,1


!==================== Solve ====================

allsel,all

!Run analysis
solve
finish

!***** Postprocessor*****
/post1


!==================== Record Temp. Profiles ====================

!Define times to record profiles
tf = tf
ts = tf/10
*dim,t,array,10
*DO,i,1,10,1
t(i)=i*ts
*ENDDO
```

```
!Define linear path to record temp profile (leg,shuttle,leg)
path,tprofile,4!6  to include bond pads
!ppath,1,,-Wp-Ll-Ws/2,-o/2,g+h/2!uncoment to include bond pad
ppath,1,,-Ll-Ws/2,-o/2,g+h/2
ppath,2,,-Ws/2,o/2,g+h/2
ppath,3,,Ws/2,o/2,g+h/2
ppath,4,,Ll+Ws/2,-o/2,g+h/2
!ppath,6,,Wp+Ll+Ws/2,-o/2,g+h/2!uncoment to include bond pad

!Save temperature data into 10 arrays for corresponding to timesteps defined
        above
SET,,,1,,t(1)
pdef,temp,temp
paget,tprof1,table

SET,,,1,,t(2)

pdef,temp,temp
paget,tprof2,table

SET,,,1,,t(3)

pdef,temp,temp
paget,tprof3,table

SET,,,1,,t(4)

pdef,temp,temp
paget,tprof4,table
```

SET,,,1,,t(5)

pdef,temp,temp
paget,tprof5,table

SET,,,1,,t(6)

pdef,temp,temp
paget,tprof6,table

SET,,,1,,t(7)

pdef,temp,temp
paget,tprof7,table

SET,,,1,,t(8)

pdef,temp,temp
paget,tprof8,table

SET,,,1,,t(9)

pdef,temp,temp
paget,tprof9,table

SET,,,1,,t(10)

pdef,temp,temp
paget,tprof10,table

```
!==================== Write Data to a File ====================

!Write temp profiles
/output,temprof.txt
*vwrite,tprof1(1,5),tprof2(1,5),tprof3(1,5),tprof4(1,5),tprof5(1,5),tprof6(1,5),tprof7(
        1,5),tprof8(1,5),tprof9(1,5),tprof10(1,5)
%16.8g %16.8g %16.8g %16.8g %16.8g %16.8g %16.8g %16.8g %16.8g %16.8g
/output

!Write x position of temp profiles
/output,temprofheaderx.txt
*vwrite,tprof1(1,1)
%16.8g
/output

!write time of temp profiles
/output,temprofheadert.txt
*vwrite,t(1)
%16.8g
/output

finish
save,all

!********** Structural Analysis **********
!resume,thermal
/filename,displacement
/prep7
dadele,all,all

!==================== Redefine Element Types ====================
```

```
et,1,92
et,2,0


!======== Define Boundry Conditions for Structural Analysis ===========

!Select Bottom Surface of Left Bond Pad
asel,s,loc,z,0
asel,r,loc,x,-Ws/2-Ll,-Ws/2-Ll-Wp

!Displacement
da,all,ux,0
da,all,uy,0
da,all,uz,0

!Select Bottom Surface of Right Bond Pad
asel,s,loc,z,0
asel,r,loc,x,Ws/2+Ll,Ws/2+Ll+Wp

!Displacement
da,all,ux,0
da,all,uy,0
da,all,uz,0

allsel,all

!============ Define Material Properties ==============
!PolySi (Mat #1)
mptemp
mp,dens,1,density
```

```
mp,ex,1,modsi
mp,prxy,1,poisson
mp,reft,1,T0
mptemp
mptgen,1,100,300,12
mp,alpx,1,thermx0,thermx1,thermx2,thermx3,thermx4

finish
allsel,all
/solu


!==================== Solution Options ====================

!Solution Type (0=Steady State, 4=Transient)
antype,4
outres,all,all
neqit,20
nlgeom,on

!Reset numbering of load steps
lswrite,init


!==================== Define Load Steps ====================

!Define durration of load steps
ls = tf/ln

!Apply temperature profiles as body loads for each load step
*DO,i,ls,tf,ls
```

```
time,i
deltim,tmin,tmin,ls/2
autots,1
ldread,temp,,,i,,thermal,rst
KBC,0
!timint,off
lswrite
*ENDDO

!Run Analysis
lssolve,1,ln,1
finish

!**** Postprocessor *****
/post26



!==================== Track a Point on Shuttle ====================

!Pick a Node on the Shuttle to Track
!nsel,s,loc,x,-Ws/2,Ws/2
!nsel,r,loc,z,g,g+h
!nsel,r,loc,y,-Wl/2,Wl/2
!*GET,numnode,node,0,num,max

kpnum = nl*4+1
ksel,s,kp,,kpnum
nslk,s
*GET,numnode,node,0,num,max
allsel,all
```

```
!Store displacement of node vs. time
nsol,2,numnode,u,y
*dim,time,array,5000
*dim,disp,array,5000
vget,time(1,1,1),1
vget,disp(1,1,1),2

!Write data to a file
/output,dispvtime.txt
*vwrite,time(1),disp(1)
%16.8g %16.8g
/output

finish
save,all
```